

Research paper

State parameter for partially drained paths using a SANISAND model

Abhinanda Dilip^{*}, Orestis Adamidis

Department of Engineering Science, University of Oxford, Parks Road, Oxford, OX1 3PJ, United Kingdom

ARTICLE INFO

Keywords:

State parameter
SANISAND
Drainage
Instability
Triaxial testing
Hostun sand

ABSTRACT

The state parameter is a fundamental component of critical state compatible, bounding surface plasticity models. Several definitions for the state parameter exist, expressing how far the current state is from critical. However, there is rarely the opportunity to directly assess the chosen state parameter definition within a given model. Here, we use a plasticity model of the SANISAND family to simulate partially drained paths in triaxial space, by imposing a constant ratio of volumetric to axial strain. We show that for such paths, the locus of post-phase transformation and post-peak stress ratio points where instability is triggered represents a constant state parameter curve in $e-p'$ space. We then present results from a series of partially drained triaxial compression experiments on Hostun sand, where volumetric and axial strains are coupled. We demonstrate that the chosen constitutive model does not recreate the experimentally observed paths well and more specifically is unable to match the experimentally obtained locus of constant state instability points. Consequently, we propose an updated state parameter definition through which the selected bounding surface plasticity model is shown to not only capture the desired locus of instability points, but to also achieve an overall improved performance in simulating partially drained paths.

1. Introduction

Though liquefaction related phenomena have been extensively studied under undrained conditions, there is mounting evidence for the importance of co-seismic drainage, its effects controlled by the nature and proximity of the relevant boundaries (e.g., Adamidis and Madabhushi, 2018; Cubrinovski et al., 2019). The effects of partial drainage can become critical for liquefaction triggering within stratified deposits, not only impacting loose sand layers but also medium to dense layers. Co-seismic upwards water flow can lead to volumetric expansion at the interface of a low-permeability layer overlying a liquefiable one, up to the point of the formation of a water film. Kokusho (1999) experimentally observed that such a water film can manifest rapidly, while Adamidis and Anastasopoulos (2022) showed that even small levels of volumetric expansion, prior to water film manifestation, are sufficient to dramatically reduce cyclic resistance. The state of the art is currently transitioning towards a more holistic view of liquefaction triggering, where stratified deposits are treated as a system of interacting layers (e.g., Cubrinovski et al., 2019; Bullock et al., 2022; Cubrinovski and Ntritsos, 2023). Partial drainage effects related to water flow and consequent local volumetric expansion can also control the triggering of instability failures, such as the seismic and post-seismic triggering of flow failures in slopes studied using centrifuge experiments by Malvick et al. (2006) and Malvick et al. (2008) and element tests by Chu et al. (2015). Reliably modelling such instability from partially drained soil

behaviour is of increasing importance for the study of liquefaction. The majority of constitutive models used for liquefaction modelling were developed based on undrained element tests, which they also depend on for calibration. Thus, assessment of their performance under partially drained conditions at an element level is required to identify shortcomings that can affect a system level analysis where drainage is important.

State-dependent bounding surface plasticity models have shown promise in capturing monotonic behaviour with coupled volumetric and shear strains. Kamai and Boulanger (2012) conducted a numerical study on the behaviour of medium to dense sands in plane strain conditions using the PM4Sand model (Boulanger and Ziotopoulou, 2015), where a constant volumetric to shear strain ratio was imposed. Their numerical results qualitatively captured experimental data. Lashkari and Yaghtin (2018) and Lashkari et al. (2021) presented an extension of the state-dependent plasticity model of Li and Dafalias (2000) to study the instability triggered in sands exhibiting fully contractive or limited-flow type behaviour under direct simple shear and triaxial compression paths, using linear, bilinear, and non-linear correlations between volumetric and shear strain. They concluded that state-dependent plasticity models better predicted coupled strain behaviour than pressure-dependent models.

This paper focuses on the importance, the definition, and the calibration of the state parameter when modelling coupled volumetric

^{*} Corresponding author.

E-mail address: abhinanda.dilip@eng.ox.ac.uk (A. Dilip).

Nomenclature

<i>CSL</i>	Critical State Line
<i>LCSI</i>	Locus of Constant State parameter Instabilities
<i>PSRS</i>	Peak Stress-Ratio State
<i>PTS</i>	Phase Transformation State
α	back-stress ratio
α^b	slope of bounding surface
α^c	slope of critical surface
α^d	slope of dilatancy surface
\dot{W}	second-order work
ΔU	excess pore pressure
$\dot{\epsilon}_1$	axial strain increment
$\dot{\epsilon}_q$	deviatoric strain increment
$\dot{\epsilon}_q^e$	elastic deviatoric strain increment
$\dot{\epsilon}_q^p$	plastic deviatoric strain increment
$\dot{\epsilon}_v$	volumetric strain increment
$\dot{\epsilon}_v^e$	elastic volumetric strain increment
$\dot{\epsilon}_v^p$	plastic volumetric strain increment
η	stress ratio ($= q/p'$)
Λ	$\dot{\epsilon}_v/\dot{\epsilon}_q$
ν	Poisson's ratio
ϕ	friction angle
ψ	state parameter ($= e - e_{cs}$)
ψ_D	updated state parameter
ζ	$\dot{\epsilon}_v/\dot{\epsilon}_1$
A_0, A_d, n^d, k^d	positive dilatancy parameters
b_{ref}	diameter of bounding surface ($\alpha^b + c \alpha^b$)
c	ratio of slope of critical surface in compression to extension
C^e	elastic compliance matrix
C^{ep}	elastoplastic compliance matrix
D	dilatancy
D^e	elastic stiffness matrix
D^{ep}	elastoplastic stiffness matrix
D_r	relative density
e	void ratio
e_0, λ, ξ	critical state line material constants
e_{INST}	void ratio at instability
e_{in}	initial void ratio
f	yield surface
G, K	elastic shear and bulk moduli, respectively
G_0, K_0	elastic moduli model parameters
h, b_0, h_0, c_h	hardening parameters
H	hardening modulus
H_L	limiting hardening modulus
I_p	pressure index
I_s	state index
m	half angular opening of the yield surface
M_{cs}	stress ratio at critical state
n^b, k^b	positive bounding parameters
p'	mean effective stress
p'_0	location of end cap in mean effective stress axis
p'_{INST}	mean effective stress at instability
p'_{in}	initial mean effective stress
p_{at}	atmospheric pressure

q	deviatoric stress
R, Q	critical state line material constants
s	' + 1' for monotonic compression, ' - 1' for monotonic extension
x, w	updated state parameter constants

to shear strain paths within the SANISAND family of bounding surface plasticity models, specifically using SANISAND 2008 (Taiebat and Dafalias, 2008). SANISAND models rely on the state parameter to control the evolution of hardening and dilatancy up to the critical state. The state parameter definition proposed by Been and Jefferies (1985) is arguably the most widely used, though other equivalent parameters have been used in literature (e.g., Dafalias and Manzari, 2004; Ishihara, 1993; Verdugo, 1992; Wang et al., 2002). Despite the state parameter being central during the calibration process of SANISAND models, its definition is not directly scrutinised. Motivated by the observation of Kamai and Boulanger (2012) in 2D space (plane strain), that coupled shear-volume softening paths in $e-p'$ relate to a constant state parameter, we examine here the existence of such constant state lines in triaxial space, with the additional aim of using them to assess the state parameter definition. We analytically demonstrate using Hill's criterion (Hill, 1958) that only instability points triggered post-phase transformation and post-peak stress ratio correspond to a state parameter that can be linked to the imposed volumetric to shear strain ratio. It should be pointed out that these instability points differ from the pre-phase transformation triggering points for flow liquefaction under volumetric expansion, as studied by Lashkari and Yaghtin (2018) and Lashkari et al. (2021). Using the locus of post-phase transformation and post-peak stress ratio instability points for a given strain coupling ratio, we show that one can recreate a constant state parameter curve. Indeed, such curves are presented in this paper, based on both simulations and on a series of coupled strain triaxial compression experiments using Hostun sand. Comparing the numerical and experimental instability loci, we demonstrate that an update to the state parameter definition is required for SANISAND 2008 to capture the experimental results. Finally, we propose an appropriately calibrated state parameter, which allows better modelling of not only the examined instability points, but of the overall behaviour through the partially drained paths.

The novel contribution of this study is twofold: first, it demonstrates a procedure for direct assessment of the state parameter within SANISAND models against experimental data; second, it shows that direct calibration of the state parameter function based on experimental data improves the overall performance of SANISAND models in replicating partially drained paths.

2. Constitutive modelling

This study employs the SANISAND 2008 model (Taiebat and Dafalias, 2008), though major findings are widely applicable within the SANISAND family.

2.1. General formulation

Only a brief description in triaxial space is given here, based on Fig. 1, as the detailed formulation can be found in Taiebat and Dafalias (2008). The model employs a narrow conical capped wedge yield surface. Plastic deformations occur when the stress state falls on the arms of the wedge or when it reaches the cap. The cap captures plastic deformations related to loading under a constant stress ratio, $\eta = q/p'$, at high confining pressures, such as due to particle grain crushing. The location of the end cap is represented by p'_0 , the isotropic hardening

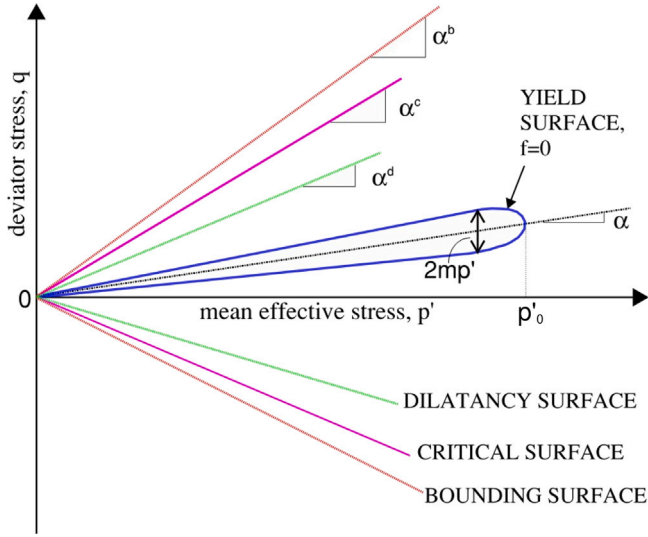


Fig. 1. Schematic illustration of model surfaces in triaxial space.
Source: Recreated from Taiebat and Dafalias (2008).

variable. The rotational hardening variable is the back-stress ratio, α , which bisects the elastic wedge. The yield surface for stress states such that $p' \ll p'_0$ is given by Eq. (1). This equation is appropriate for this paper, as liquefaction studies are conducted at low confining pressure range, where particle crushing is typically not considered (e.g. Andrianopoulos et al., 2010; Kassas et al., 2021; Taiebat et al., 2010; Yang et al., 2022; Petalas et al., 2019). As liquefaction is triggered through gradual reduction in effective stresses, p' remains $\ll p'_0$ and particle crushing does not contribute significantly to the plastic strains and strength characteristics. So the end cap of the yield surface that captures crushing related plastic strains at high confining pressures, remains inactivated throughout the numerical simulations conducted in this study. The value of m represents half the angular opening of the elastic wedge.

$$f = |\eta - \alpha| - m = 0 \quad (1)$$

The bounding surface, α^b relates to the peak stress ratio and the dilatancy surface, α^d relates to the phase transformation stress ratio. The two surfaces evolve based on the critical surface, α^c and the state parameter, ψ , their evolution controlled by Eqs. (2) and (3), where n^b and n^d are positive model parameters. Alternate expressions based on a linear dependency on the state parameter have also been used, as shown in Eqs. (2) and (3) where k^b and k^d are positive model parameters (e.g., Manzari and Dafalias, 1997). For loading in triaxial extension, the same relations apply, albeit with a reduced slope of the critical surface, given by $c \alpha^c$. The critical state line (CSL) in $e-p'$ space is given by Eq. (4), where e_0 , λ and ξ are material constants and p_{at} is the atmospheric pressure. The state parameter definition by Been and Jefferies (1985) is adopted as a measure of the distance between the current void ratio, e and the critical state void ratio, e_{cs} at the current mean effective stress (Eq. (5)). At the critical state, the bounding and dilatancy surfaces collapse on the critical surface as $\psi \rightarrow 0$.

$$\alpha^b = \alpha^c \exp(-n^b \psi) \quad \text{or} \quad \alpha^b = \alpha^c - k^b \psi \quad (2)$$

$$\alpha^d = \alpha^c \exp(n^d \psi) \quad \text{or} \quad \alpha^d = \alpha^c + k^d \psi \quad (3)$$

$$e_{cs} = e_0 - \lambda (p'/p_{at})^\xi \quad (4)$$

$$\psi = e - e_{cs} \quad (5)$$

The elastic response follows the hypo-elastic assumption, with the shear modulus (G) and the bulk modulus (K) given in Eqs. (6) and (7), respectively. G_0 and K_0 are positive model parameters. Alternately, as is common practice, one modulus can be derived from the other using a constant Poisson's ratio, ν (Eq. (8)).

$$G = G_0 p_{at} \frac{(2.97 - e)^2}{1 + e} \left(\frac{p'}{p_{at}} \right)^{\frac{1}{2}} \quad (6)$$

$$K = K_0 p_{at} \frac{(1 + e)}{e} \left(\frac{p'}{p_{at}} \right)^{\frac{2}{3}} \quad (7)$$

$$K = \frac{2(1 + \nu)}{3(1 - 2\nu)} G \quad (8)$$

The elastic and plastic strain increments for $p' \ll p'_0$ are given in Eqs. (9)–(10) and (11)–(12), respectively, with s representing the loading direction: $' + '1$ for compression and $' - '1$ for extension. The hardening modulus, H controls the kinematic hardening, its value dependent on the relative distance between the bounding surface and the current stress ratio, as outlined in Eq. (13), with h_0 and c_h positive model parameters and b_{ref} the diameter of the bounding surface. Similarly, dilatancy D is a function of the relative distance between the dilatancy surface and the current stress ratio, as shown in Eq. (14), where A_d is a positive dilatancy parameter. The linear function $h_0(1 - c_h e)$ in Eq. (13) can be replaced with an exponential function $h_0 \exp(-c_h e)$ to achieve a better fit to experimental results (Taiebat and Dafalias, 2008).

$$\text{Elastic volumetric strain : } \dot{\epsilon}_v^e = \frac{\dot{p}'}{K} \quad (9)$$

$$\text{Elastic deviatoric strain : } \dot{\epsilon}_q^e = \frac{\dot{q}}{3G} \quad (10)$$

$$\text{Plastic volumetric strain : } \dot{\epsilon}_v^p = \frac{\dot{\alpha} D}{H} \quad \text{or} \quad D |\dot{\epsilon}_q^p| \quad (11)$$

$$\text{Plastic deviatoric strain : } \dot{\epsilon}_q^p = \frac{\dot{\alpha} s}{H} \quad (12)$$

$$H = h(\alpha^b - \alpha); \quad \text{where } h = \frac{b_0}{(b_{ref} - s(\alpha^b - \alpha))^2} \quad \text{and}$$

$$b_0 = G_0 h_0 (1 - c_h e) \left(\frac{p_{at}}{p'} \right)^{\frac{1}{2}} \quad (13)$$

$$D = s A_d (\alpha^d - \alpha) \quad (14)$$

Using the model equations, the elastic stiffness matrix (D^e) and the elastoplastic stiffness matrix (D^{ep}) are obtained for $p' \ll p'_0$, as shown in Eqs. (15) and (16), respectively. The elastic compliance matrix C^e and elasto-plastic compliance matrix C^{ep} are shown in Eqs. (17) and (18), respectively.

$$D^e = \begin{bmatrix} K & 0 \\ 0 & 3G \end{bmatrix} \quad (15)$$

$$D^{ep} = \begin{bmatrix} \frac{p' H K + 3 G K s}{p' H + 3 G s - D K \eta} & \frac{-3 G K D}{p' H + 3 G s - D K \eta} \\ \frac{3 G K \eta s}{p' H + 3 G s - D K \eta} & \frac{3 G p' H - 3 G K D \eta}{p' H + 3 G s - D K \eta} \end{bmatrix} \quad (16)$$

$$C^e = \begin{bmatrix} 1/K & 0 \\ 0 & 1/3G \end{bmatrix} \quad (17)$$

$$C^{ep} = \begin{bmatrix} \frac{1}{K} - \frac{D \eta}{p' H} & \frac{D}{p' H} \\ \frac{-\eta s}{p' H} & \frac{1}{3G} + \frac{s}{p' H} \end{bmatrix} \quad (18)$$

2.2. Numerical simulations of coupled strain monotonic paths

The SANISAND 2008 model in triaxial space was numerically implemented in MATLAB using the forward Euler method and strain-controlled steps. The model parameters for Toyoura sand listed in Table 1 were used, with $m = 0.05 \alpha^c$. Coupled strain triaxial compression tests were numerically simulated, where constant ratios of

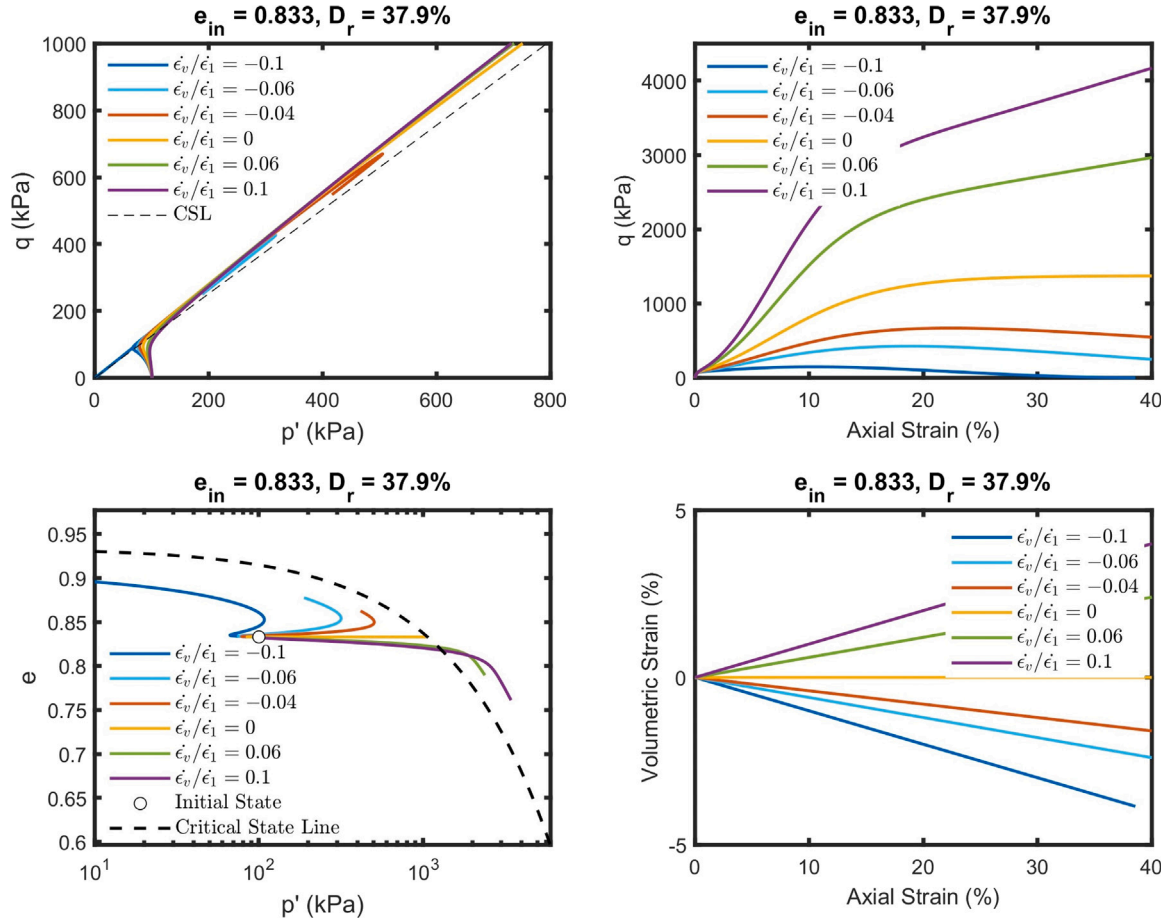


Fig. 2. Simulations for coupled strain paths on isotropically consolidated samples of Toyoura sand in triaxial space for varying strain ratios ϵ_v/ϵ_1 (relative density, $D_r = 37.9\%$ and initial mean effective stress, $p'_{in} = 100$ kPa).

Table 1
SANISAND model parameters for Toyoura sand (Taiebat and Dafalias, 2008).

Parameter	Parameter	Parameter	Parameter
G_0 (kPa)	125	e_0	0.934
K_0 (kPa)	150	λ	0.019
α^c	1.2	ξ	0.7
		A_d	0.4
		n^d	2.1
		h_0	36.96
		c_h	0.987
		n^b	1.25
		c	0.712

volumetric strain increment (ϵ_v) to axial strain increment (ϵ_1) were imposed, with positive volumetric strain indicating contraction. Indicative results for a specimen of $D_r = 37.9\%$ and for a range of coupling strain ratios, including the undrained condition, are shown in Fig. 2.

Researchers have previously experimentally explored sand response under coupled strain loading paths (Vaid and Eliadorani, 1998, 2000; Lancelot et al., 2004; Nicot et al., 2013; Sivathayalan and Logeswaran, 2008; Chu et al., 2015). Numerical simulations of coupled strain path tests have also been presented in literature, using critical state compatible models in plane strain space (Lashkari et al., 2021; Kamai and Boulanger, 2012) and in triaxial space (Lashkari and Yaghtin, 2018). Experimental findings and simulation results match well with the paths shown in Fig. 2. The undrained path of Fig. 2 undergoes strain-hardening. Under water outflow conditions ($\epsilon_v/\epsilon_1 > 0$), more significant strain-hardening is observed, bringing q to higher values than under undrained loading. The combined effect of dilation and water outflow, increase p' , leading the path beyond the CSL in $e - p'$ space. Note that the imposed coupled strain conditions do not allow critical state to ever be reached. Under water inflow conditions ($\epsilon_v/\epsilon_1 < 0$), initial strain hardening is followed by post-peak strain softening down to $q = 0$, a behaviour indicative of a flow liquefaction failure. The

path in $e - p'$ space never reaches the CSL. During the strain-softening response, the effect of water inflow can no longer be counteracted by dilation, signifying that instability triggering and flow liquefaction are possible under water inflow conditions, even for soils that display a stable response under undrained conditions. For loose-of-critical specimens subjected to water inflow, strain softening becomes even more pronounced than under undrained conditions. On the contrary, water outflow can prevent liquefaction manifestation for such specimens.

3. Instability triggering under coupled strain paths

Here, the process of using coupled strain paths to isolate and examine the state parameter function, ψ (Eq. (5)), is presented. This analysis was motivated by the coupled strain 2-D numerical results of Kamai and Boulanger (2012) using the PM4SAND model (Boulanger and Ziotopoulou, 2015). Kamai and Boulanger (2012) simulated dilative specimens under water inflow conditions and found that the resulting strain softening branch in $e - p'$ space relates to a constant state parameter. In the following section, we investigate the existence of such a constant state parameter curve in triaxial space and demonstrate that it corresponds to the locus of post-phase transformation and post-peak stress ratio instability triggering points, obtained under the same strain coupling ratio. A maximum of one such point can be identified for each partially drained path.

3.1. Instability assessment

Instability triggering is associated with a loss of uniqueness of the incremental response under a particular loading programme. A

unique incremental response under a loading programme can be ensured as long as the matrix relating the responding variables to the controlled variables remains invertible. For example, in a purely strain-controlled triaxial test, a non-unique incremental response is expected when the determinant of the elastoplastic compliance matrix (Eq. (18)) becomes zero: $\det[C^{ep}] = 0$. Imposing this condition on the SANISAND 2008 constitutive model (Taiebat and Dafalias, 2008), the modulus of critical softening H_c (Imposimato and Nova, 1998) can be obtained where $H_c = (3Gs - DK\eta)/p'$ such that when the hardening modulus $H = -H_c$, an instability is triggered. Such an instability under a purely strain-controlled condition is rarely encountered in physical testing (Imposimato and Nova, 1998). Indeed, H remains greater than $-H_c$ throughout the strain-controlled tests examined here.

In reality, multiple loss-of-uniqueness loci exist in the deviatoric plane, some of which can be physically discerned by a loss of test controllability (Imposimato and Nova, 1998). The loss of uniqueness for purely stress controlled loading was called the 'limit locus' where the stiffness matrix, as shown in Eq. (16), no longer remains invertible ($\det[D^{ep}] = 0$). For the SANISAND 2008 constitutive model (Taiebat and Dafalias, 2008) under a pure stress controlled loading, the hardening modulus vanishes at the 'limit locus' ($\det[D^{ep}] = 3GKH/(H + H_c)$). Imposimato and Nova (1998) concluded that the positive definiteness of the second-order work (Hill, 1958) is a necessary and sufficient condition to ensure a unique material response under any combination of mixed stress-strain control loading programmes.

The findings of Imposimato and Nova (1998) were supported by Andrade (2009) and Andrade et al. (2013), who numerically simulated undrained behaviour under monotonic compression in triaxial space, using the Nor-Sand model (Jefferies, 1993) and the Dafalias and Manzari (2004) predecessor of the SANISAND family, respectively. They imposed a loss of uniqueness condition and Hill's stability criterion (Hill, 1958) to detect the onset of instability under a deviatoric stress rate (\dot{q}) in undrained compression tests and proved the coincidence of the two approaches. Using Hill's condition, Andrade et al. (2013) further related the slope of the instability line in stress ratio ($q - p'$) space to a limiting hardening modulus that was found to be a function of the soil state. The onset of instability under coupled strain path simulations has been similarly evaluated using Hill's stability criterion (Lashkari and Yaghtin, 2018; Lashkari et al., 2021).

Here, the instability point being pursued pertains to a hypothetical mixed stress and strain controlled loading programme, where the deviatoric stress increment (\dot{q}) and the volumetric strain increment ($\dot{\epsilon}_v$) are controlled with a condition that the ratio of the volumetric to deviatoric strain increment remains a constant ($\dot{\epsilon}_v/\dot{\epsilon}_q = \Lambda$). Imposing a loss of uniqueness criterion to the SANISAND 2008 constitutive model (Taiebat and Dafalias, 2008), an expression for the hardening modulus was derived such that when the condition of Eq. (19) is achieved, an instability is triggered. One possible point of instability satisfying Eq. (19) is attained when the dilatancy $D = s\Lambda$ and the hardening modulus $H = 0$. It should be pointed out that the numerical simulations performed in this paper were fully strain-controlled and as such are expected to remain stable at the mixed control instability of Eq. (19).

$$H = (D - s\Lambda)\eta K / p' \quad (19)$$

3.2. Criterion for instability under coupled strain paths

Following the conclusion of Imposimato and Nova (1998), Hill's stability criterion (Hill, 1958) was implemented in this study to detect the onset of instability under coupled strain paths in triaxial space. Andrade et al. (2013) deduced the second-order work, \dot{W} in triaxial space as a function of the increments of mean effective stress (\dot{p}'), deviator stress (\dot{q}) and strains ($\dot{\epsilon}_v$ and $\dot{\epsilon}_q$) and imposed Hill's condition to obtain Eq. (20), which is a condition for stability under any loading programme.

$$\dot{W} = \dot{p}'\dot{\epsilon}_v + \dot{q}\dot{\epsilon}_q > 0 \quad (20)$$

When applied to the undrained case under strain-controlled monotonic compression loading, $\dot{q} \leq 0$ at instability. Hence, the onset of instability in loose sand specimens under undrained conditions occurs at the peak of the stress path in $q - p'$ space, when $\dot{q} = 0$. This instability can be physically detected under a mixed stress-strain controlled experiment where $\dot{\epsilon}_v = 0$ and $\dot{q} > 0$ are imposed. There may be temporary instability for dense and medium dense sands under undrained loading, where $\dot{q} \leq 0$ and the soil undergoes limited flow liquefaction, until the phase transformation stress ratio is reached. After phase transformation, the sand dilates with $\dot{q} > 0$ until the critical state, where $\dot{q} = 0$, indicating the final instability point.

An expression for the second-order of work from Hill's stability criterion in triaxial space, shown in Eq. (20), was obtained under a condition of $\dot{\epsilon}_v/\dot{\epsilon}_q = \Lambda$, using the elastoplastic constitutive relation of SANISAND 2008 (Eq. (16)). Instability was detected when the second-order of work changed from positive to negative or vanished at large strains. Alternatively, a limiting hardening modulus (H_L) determining the onset of instability can be derived, generalising the undrained loading relation obtained by Andrade et al. (2013), so that it applies for any ratio of volumetric strain increment to axial strain increment ($\zeta = \dot{\epsilon}_v/\dot{\epsilon}_1$):

$$H_L = \frac{3GK(D - s\Lambda)(\eta + \Lambda)}{p'(K\Lambda^2 + 3G)} \quad (21)$$

$$\Lambda = \frac{\dot{\epsilon}_v}{\dot{\epsilon}_q} = \frac{3\zeta}{3 - \zeta} \quad (22)$$

Fig. 3 shows the instability points detected using Hill's condition (Eq. (20)) for three element simulations of medium dense - dense Toyoura sand under initial mean effective stress, $p'_{in} = 100$ kPa and $\zeta = -10\%$. The second-order of work instability, as shown in Fig. 3(d), coincides with the point where the limiting hardening modulus first exceeds the hardening modulus, $H_L \geq H$, as shown in Fig. 3(e). Note that Eq. (21) reduces to Eq. (19) for $|\eta| \gg \Lambda$ and $3G \gg K\Lambda^2$.

3.3. Isolation of state parameter from instability points

It is worth noting that in Fig. 3(e), the limiting hardening modulus, $H_L \approx 0$ and the hardening modulus, $H \approx 0$ at the instability points. From Eq. (21), it can be deduced that for this to happen, either the dilatancy, $D \approx \Lambda$ (as $s = +1$ for monotonic compression) or the stress ratio, $\eta \approx -\Lambda$. As seen from the $q - p'$ plots of Fig. 3(a), η is close to or greater than unity at the detected instability points. Hence, it is dilatancy, D that must become equal to Λ . Indeed, this is demonstrated in Fig. 3(f), where the curves depicting the evolution of dilatancy intersect a dashed, constant Λ line at the points of instability.

Drawing from these observations, using Eq. (2)–(3), (13)–(14), (21)–(22), and taking $s = +1$ for monotonic compression, the following can be concluded at the identified instability points:

$$H_L \approx 0 \Rightarrow D - s\Lambda \approx 0 \Rightarrow D \approx \Lambda \quad (23)$$

$$H \approx 0 \Rightarrow h(\alpha^b - \alpha) \approx 0 \Rightarrow \alpha^b \approx \alpha \quad (24)$$

$$D \approx \Lambda \Rightarrow sA_d(\alpha^d - \alpha) \approx \Lambda \Rightarrow A_d(\alpha^d - \alpha^b) \approx \Lambda \quad (25)$$

$$\Rightarrow A_d\alpha^c(e^{n^d\psi} - e^{-n^b\psi}) \approx \frac{3\zeta}{3 - \zeta} \quad (26)$$

If linear expressions are used for the bounding and dilatancy stress ratios as functions of ψ , (Eqs. (2) and (3)), Eq. (26) becomes Eq. (27), which is preferential in terms of parameter calibration under partially drained conditions and will be used here.

$$A_d(k^d\psi + k^b\psi) \approx \frac{3\zeta}{3 - \zeta} \quad (27)$$

Eq. (27) represents the locus of identified instability triggering points under a constant strain increment ratio, ζ . In Eq. (27), the only variable on the left hand side is the state parameter, ψ , which must have a specific value for a given strain coupling ratio ζ on the right hand side. Consequently, for a given ζ , the locus of the identified instability points corresponds to a constant ψ curve.

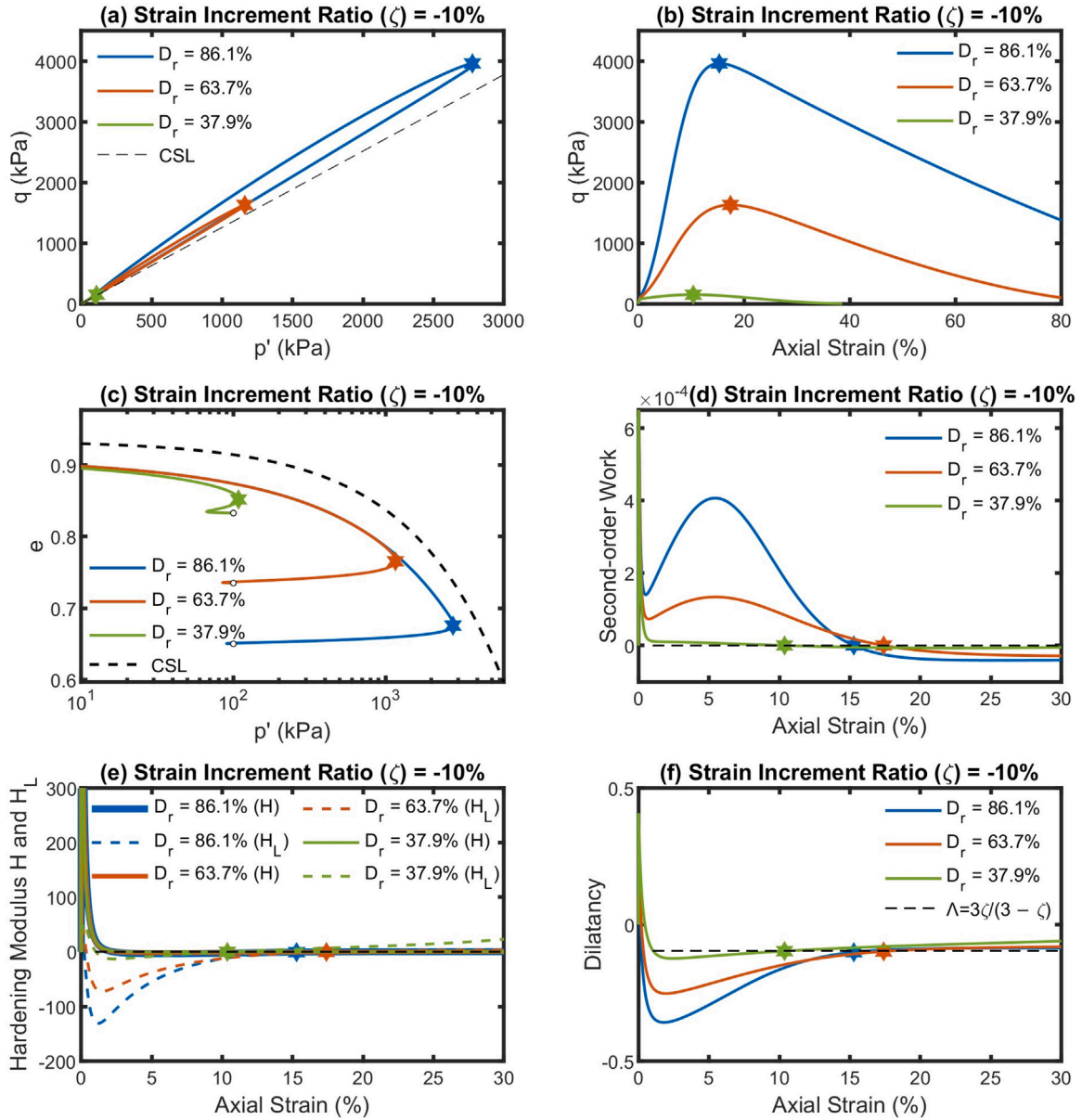


Fig. 3. Simulations for coupled strain paths on isotropically consolidated samples of Toyoura sand in triaxial space for $\zeta = -10\%$ and $p'_{in} = 100$ kPa; instability points are shown in star markers.

3.4. Applicability of the proposed instability locus

Though all instability triggering points of Fig. 3 corresponded to the same state parameter, this is not true for instability triggering points in general. The following two conditions must be met for instability triggering points under a given coupling ratio ζ to correspond to a specific state parameter ψ :

$$\text{Condition 1: } H = H_L \text{ with } \dot{H}_L \geq \dot{H} \quad (28)$$

This condition is a direct consequence of the Hill's stability criterion (Eq. (20)). At the onset of instability, $H = H_L$. Loss of stability implies that H_L exceeds H , hence the rate inequality above, indicating a point of instability triggering, rather than the transition from an unstable to a stable region.

$$\text{Condition 2: } H \approx 0 \text{ and } H_L \approx 0 \quad (29)$$

Condition 1 indicates instability triggering, but Condition 2 is also required to derive Eq. (27) that allows the isolation of the state parameter. If both conditions apply for a coupled strain compression test,

the point located triggers a final instability, rather than a temporary one. The locus of all such instability points for a particular coupled strain ratio satisfying Conditions 1 and 2 is therefore named the Locus of Constant State parameter Instabilities (LCSI).

As aids to this section, simulations of monotonic triaxial compression tests for a range of initial densities under a strain coupling ratio, $\zeta = -2.5\%$ are presented in Fig. 4, using the parameters of Table 1. Instability points were obtained using Hill's condition (Eq. (20)), as shown in Fig. 4(b). The instability points that satisfy Condition 1 are shown with filled circles and the instability points satisfying both Conditions 1 and 2 are shown with filled stars.

If both Conditions 1 and 2 are met, Eq. (23) holds. As the strain increment ratio ζ (or Λ) < 0 for water inflow conditions, the dilatancy parameter $D \approx \Lambda < 0$ at the instability point, as seen for the two denser soils of Fig. 4(d). This implies that the soil must undergo phase transformation, i.e., the back-stress ratio α must cross the dilatancy surface α^d prior to attaining instability (Eq. (14)). For the undrained case, the dilatancy parameter $D \approx \Lambda \approx 0$ at the instability point. The two specified conditions cannot be satisfied by contractive soils,

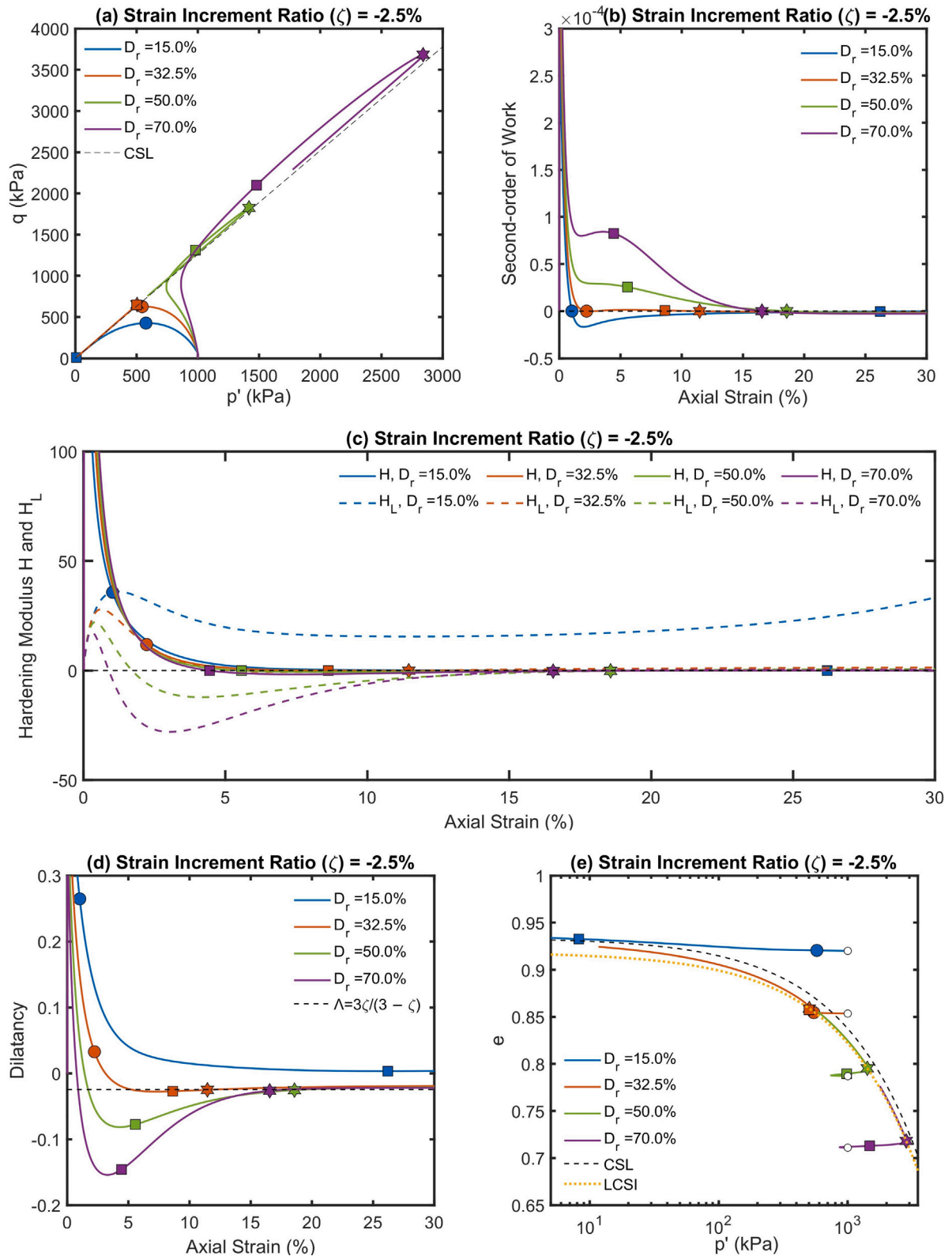


Fig. 4. Simulations for triaxial compression tests on isotropically consolidated samples of Toyoura sand under $\zeta = -2.5\%$ with the initial states shown in white circles, instability points satisfying Condition 1 shown in solid filled circles, peak stress ratio shown in solid filled squares and instability points satisfying Conditions 1 and 2 shown in solid filled star markers.

where $D > 0$. This is confirmed from Fig. 4(d) for the soil with initial $D_r = 15.0\%$. Thus, the locus of the instability points we are pursuing here cannot be attained for soils that only show contractive behaviour under the imposed coupled strain path. For soils undergoing phase

transformation, the peak stress ratio state ($H = 0$), shown in solid filled squares, is reached post-phase transformation and post the maximum magnitude negative dilatancy point, as seen in Figs. 4(c) and 4(d). Thus, the hardening modulus $H > 0$ at the phase transformation point,

Table 2

Sign transition of hardening modulus, H , limiting hardening modulus, H_L and dilatancy, D under incremental coupled strain monotonic compression tests for medium dense to dense sands.

Test stage	H	H_L	D	Remarks
Before Phase Transformation	'+' ve	'+' ve	'+' ve	$H > H_L$
At Phase Transformation	'+' ve	0 or $\rightarrow 0$	0	$H_L = 0$ for undrained; $H > H_L$
PTS to Peak Stress Ratio	'+' ve	'-' ve	'-' ve	$H > H_L$
At Peak Stress Ratio	0	'-' ve	'-' ve	H_L and D are near minimum ' - ' ve value
Post-Peak Stress Ratio	'-' ve	'-' ve	'-' ve	H_L and D increase towards 0
At Instability	$\rightarrow 0$	$\rightarrow 0$	'-' ve	$H = H_L \approx 0$; $D \approx \Lambda$

indicating that the back-stress ratio α is yet to cross the bounding surface α^b (Eq. (13)).

From Eq. (21), it can be inferred that under an inflow condition, the limiting hardening modulus H_L becomes negative when $D < \Lambda$ and remains negative at the peak stress ratio. H_L achieves a minimum negative value at the maximum magnitude negative dilatancy point, see Fig. 4(c). Overall, at the phase transformation point, $H > 0$ and $H_L = 0$ under an undrained condition, while $H > 0$ and H_L is greater than but close to 0 under an inflow condition. In both cases, $H > H_L$. At the peak stress ratio, $H = 0$ and $H_L < 0$, so that still $H > H_L$. Thus, the instability points that satisfy the conditions outlined at the beginning of this section are expected to occur post-phase transformation and post-peak stress ratio. If a specimen fails before these conditions, then it is not possible for it to attain the instability necessary to isolate a state parameter value. Table 2 summarises the evolution of the hardening modulus, the limiting hardening modulus and the dilatancy parameter under coupled strain paths for dilative soils.

For the undrained case, the LCSi is represented by the CSL, where $\psi = 0$ (Eq. (26)), while for water inflow conditions, the LCSi is represented by a constant $\psi < 0$ curve as shown in Fig. 4(e). For the fully contractive soil state ($D_r = 15.0\%$), the instability points satisfy only Condition 1 and do not fall on the LCSi. As seen in Figs. 4(a) and 4(e), for the soil states undergoing phase transformation, the instability points satisfying both Conditions 1 and 2 occur after the peak stress ratio state, and fall on the LCSi. A temporary instability point satisfying only Condition 1 but with $H > 0$ and $D > 0$ may be encountered for medium dense initial states prior to undergoing phase transformation. Such a point represents the onset of a limited liquefaction behaviour and does not lie on the LCSi. Post-phase transformation, a second instability point that satisfies both conditions and lies on the LCSi can be achieved for such tests, as in the case of $D_r = 32.5\%$ in Fig. 4. Finally, for the dense specimens, $D_r = 50.0\%$ and 70.0% , both conditions are met at the instability point since $H = H_L \approx 0$ (Fig. 4(c)). Consequently, the instability point lies on the LCSi in Fig. 4(e).

3.4.1. Verification of proposed instability line

Having established the applicability of the LCSi in Section 3.4, Eq. (26) is plotted for Toyoura sand in the $e - p'$ space in Fig. 5 for three strain coupling ratios. Simulated paths from a range of initial states under the imposed coupling ratios are plotted and the instability points derived from Eq. (20) and satisfying Conditions 1 (Eq. (28)) and 2 (Eq. (29)) are added as star markers. As seen from Fig. 5, Eq. (26) defines the instability points accurately across a range of initial conditions and ζ values. This theoretical exercise shows that triaxial compression tests performed under a given strain coupling ratio ζ can be used to determine the locus of constant state instability points (LCSi), which for a bounding surface plasticity model of the SANISAND family lie on a constant state parameter ψ curve (Eqs. (26) or (27)).

4. Hostun sand calibration

An experimental campaign was performed using coupled strain triaxial compression tests on Hostun HN31 sand to identify the LCSi and through it assess the currently used definition of the state parameter for SANISAND 2008 (Taiebat and Dafalias, 2008). An initial calibration was based on the series of drained and undrained monotonic triaxial compression tests described below.

Table 3

Properties of Hostun Sand.

e_{max}	e_{min}	d_{50}	C_u	C_c	G_s
0.993	0.647	355 μ m	1.79	0.99	2.65

e_{max} = maximum void ratio; e_{min} = minimum void ratio;
 d_x = particle size for which (x)% of the material is finer;
 $C_u = d_{60}/d_{10}$ coefficient of uniformity;
 $C_c = d_{30}^2/(d_{10} \times d_{60})$ coefficient of curvature;
 G_s = specific gravity of solids.

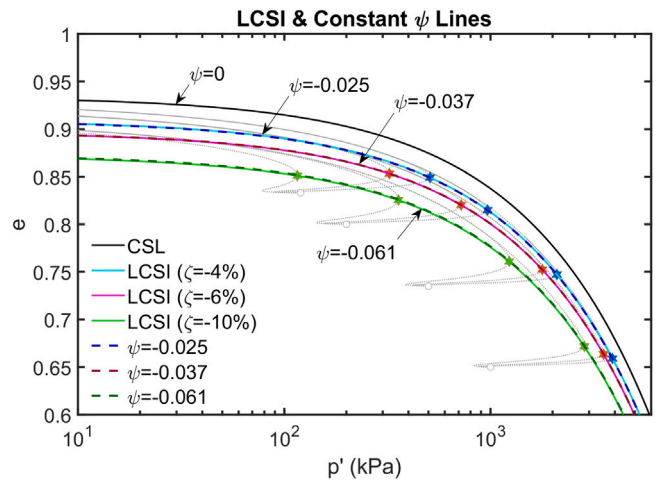


Fig. 5. Locus of Constant State Parameter Instability points (LCSi) or Constant ψ Lines for coupled strain paths in triaxial space on Toyoura sand under $\zeta = -4\%$, -6% and -10% .

4.1. Experimental testing

The experiments were performed using a GDS advanced dynamic triaxial testing device at the University of Oxford. The tests presented here were conducted under strain controlled monotonic compression loading. A sketch of the testing device is given in Fig. 6. All tests were performed using Hostun HN31 sand, which is widely used in Europe for liquefaction-related studies. It is a uniformly graded fine sand comprising of sub-angular to angular siliceous particles. The sand properties obtained from physical characterisation tests conducted at the University of Oxford are listed in Table 3. The limiting void ratios were measured according to the Norwegian Geotechnical Institute (NGI) standards. The properties obtained for the sand differ slightly from the values reported by Kassas et al. (2021) and Adamidis and Anastasopoulos (2022), who used different batches of Hostun sand. However, they fall within the range reported from various testing facilities as listed by Azeiteiro et al. (2017).

4.1.1. Testing protocol

The testing protocol was based on ASTM D4767-11R20 for undrained tests and ASTM D7181-20 for drained tests. Cylindrical specimens measuring 70 mm diameter and 140 mm height were prepared using the water (wet) pluviation technique. A back pressure of

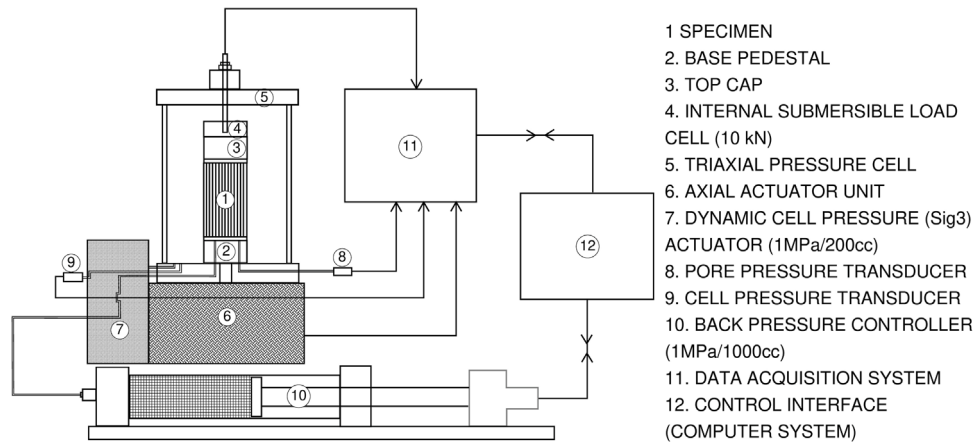


Fig. 6. Diagram of GDS advanced dynamic triaxial testing device at University of Oxford.

Table 4

Results of monotonic triaxial tests performed at University of Oxford.

Test ID ^a	e_{in}^b	p'_{in}^b	e_{end}	p'_{end}	η_{PTS}^c	ϕ_{PTS}^c	η_{PSRS}^d	ϕ_{PSRS}^d	η_{end}	ϕ_{end}
ICUMC/0.832/100 (U1)	0.832	100	0.832	302.8	1.24	30.9°	1.36	33.6°	1.31	32.5°
ICUMC/0.828/300 (U2)	0.828	300	0.828	974.9	1.14	28.6°	1.31	32.6°	1.13 ^e	28.5°
ICUMC/0.874/300 (U3)	0.874	300	0.874	499.9	1.27	31.5°	1.34	33.2°	1.17 ^e	29.3°
ICUMC/0.736/300 (U4)	0.736	300	0.736	1331.9	1.22	30.4°	1.43	35.3°	1.40 ^f	34.6°
ICUMC/0.718/300 (U5)	0.718	300	0.718	1583.1	1.25	31.2°	1.44	35.4°	1.39 ^e	34.4°
ICUMC/0.790/300 (U6)	0.790	300	0.790	1114.3	1.20	29.9°	1.36	33.7°	1.09 ^e	27.4°
ICUMC/0.896/10 (U7)	0.896	10	0.896	215.04	1.28	31.9°	1.47	36.1°	1.10	27.7°
ICDMC/0.784/300 (D1)	0.784	300	0.830	504.7	–	–	1.43	35.4°	1.19	29.7°
ICDMC/0.821/100 (D2)	0.821	100	0.884	177.2	–	–	1.47	36.1°	1.22	30.4°
ICDMC/0.827/200 (D3)	0.827	200	0.845	331.8	–	–	1.37	33.9°	1.15	28.8°
ICDMC/0.842/100 (D4)	0.842	100	0.885	170.8	–	–	1.42	35.0°	1.14	28.7°
ICDMC/0.869/20 (D5)	0.869	20	0.909	39.8	–	–	1.45	35.8°	1.11	27.8°
ICDMC/0.812/20 (D6)	0.812	20	0.881	36.7	–	–	1.44	35.5°	0.98	25.0°
ICDMC/0.874/12 (D7)	0.874	12	0.913	24.2	–	–	1.46	35.8°	0.91	23.3°
ICDMC/0.865/150 (D8)	0.865	150	0.872	241.4	–	–	1.35	33.4°	1.09	27.4°

^a (1) type of consolidation: IC or K0 for isotropic or anisotropic consolidation, respectively; (2) type of drainage: D for drained, U for undrained and PD for partially drained; (3) type of loading: MC or ME for monotonic compression or monotonic extension; (4) void ratio immediately after consolidation; and (5) mean effective stress immediately after consolidation.

^b Post consolidation values;

^c PTS: Phase transformation state;

^d PSRS: Peak stress ratio state;

^e The test reached critical state;

^f Load cell maximum capacity attained just before critical state.

–10 kPa was applied and maintained during dismantling of the split mould and filling of the triaxial cell. The B-values for all tests were greater than 96%. The specimens were isotropically consolidated to the required mean effective stress, p'_{in} . Strain controlled monotonic compression was imposed with axial displacement rates of 6 mm/hr for undrained tests and 3 mm/hr for drained tests, up to a maximum of 35% axial strain. Membrane correction and parabolic barrelling were considered according to Lade (2016). Membrane penetration effects calculated based on Lade (2016) were found to be negligible due to low effective cell pressures (cell pressure - pore pressure \leq 300 kPa) and small particle size.

4.1.2. Monotonic triaxial test results

Table 4 summarises the monotonic tests performed for calibration. Fig. 7 includes all tests of Table 4, plotted in red in $e - p'$ space, along with a proposed CSL. As seen in the figure, none of the drained tests were able to reach the CSL whereas 4 out of 7 undrained tests did reach it. A test was deemed to have reached the CSL based on the flattening of the excess pore pressure curve for undrained tests and the flattening of the volumetric strain curve for drained tests. Phase transformation states (PTS) were detected when mean effective stress p' was minimised in undrained tests. Peak stress ratio states (PSRS) were

obtained at the maximum stress ratio η point in drained and undrained tests. The proposed expression for the CSL was based on the tests listed in Table 4 and shown in red paths in Fig. 7. Tests conducted on a different batch of Hostun HN31 are also shown in grey (see Adamidis and Anastasopoulos (2022) for information on experimental methods for these tests). Previous tests reaching the CSL using Hostun HN31 are included, as published by Azeiteiro et al. (2017) and Konrad (1993). Though all tests were performed on nominally the same sand, different batches were used each time. To account for variability in maximum and minimum void ratios, relative density D_r is used in Fig. 7. The proposed CSL for Hostun sand is given in Eq. (30) and shown in purple in Fig. 7. It follows the form proposed by Bolton (1986). The CSL proposed here is steeper at high levels of p' compared to the one proposed by Azeiteiro et al. (2017), included in green in Fig. 7.

Note that Eq. (30) is applicable for critical void ratios $\geq e_{min}$. To account for critical void ratios $< e_{min}$, breakage related broadening of the particle size gradation needs to be considered through additional testing to locate the CSL appropriately at higher confining pressures. Increased particle crushing upon continued shearing at higher confining pressures results in lowering of the CSL, the evolution of which has been incorporated in constitutive models in literature, using a grading state index or by considering a dynamic reference line (e.g. Kikumoto

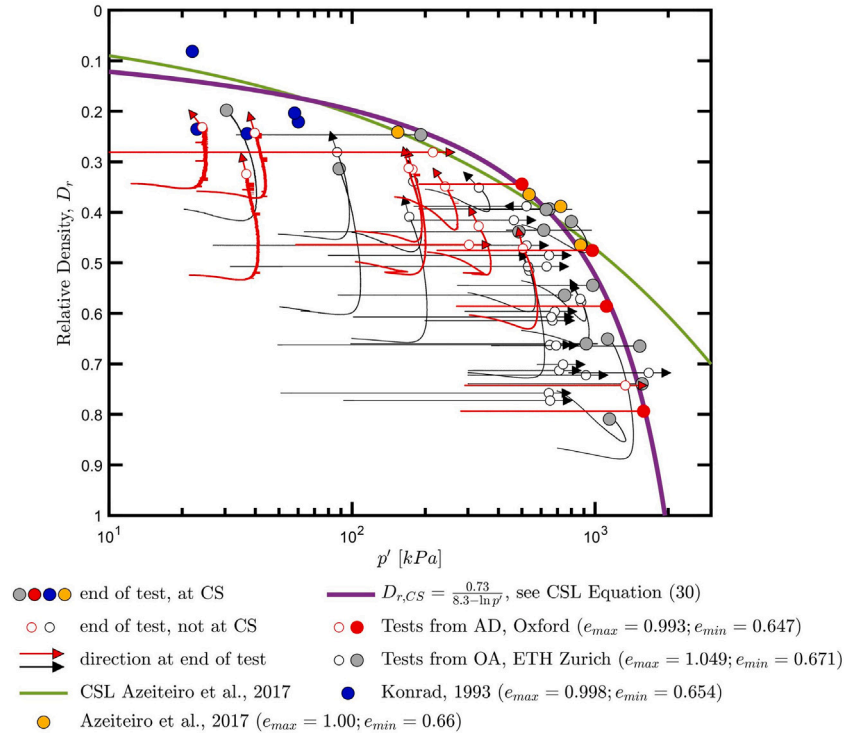


Fig. 7. Critical state line for Hostun sand.

et al., 2010; Yao et al., 2009, 2019). The current study is aimed at numerical modelling of liquefaction triggering phenomena for silica sands, which occur at low confining pressures and where particle crushing is typically not considered (e.g. Andrianopoulos et al., 2010; Taiebat et al., 2010; Kassas et al., 2021; Petalas et al., 2019; Yang et al., 2022). As such, the effect of particle breakage at higher confining pressures has not been taken into account within the scope of this work.

$$e_{cs} = e_{max} - \frac{(e_{max} - e_{min})R}{Q - \ln(p')} \quad (30)$$

where e_{cs} = void ratio at critical state; $e_{max} = 0.993$; $e_{min} = 0.647$; $R = 0.73$ and $Q = 8.3$

4.2. Elastic moduli

The small-strain shear modulus, G_{max} as obtained by Azeiteiro et al. (2017) using bender element tests on air-pluviated triaxial samples of Hostun sand, is shown in Eq. (31) and follows the form proposed by Hardin (1978). This expression was obtained from specimens at two different initial densities and a unique mean effective stress level.

$$G_{max} = G_0 p_{at} \frac{(2.97 - e)^2}{1 + e} \left(\frac{p'}{p_{at}} \right)^{0.49} \quad \text{where} \quad G_0 = 293 \quad (31)$$

At ETH Zurich, bender element tests on wet-pluviated triaxial specimens of Hostun sand were conducted at four initial densities, each isotropically consolidated to five different levels of confining stress. Eq. (31) was found to match the stiffness results for three densities (Kassas et al., 2021) but underestimated the value for the densest specimen. An expression for G_{max} resulting from the bender element tests was proposed as shown in Eq. (32) which has been used in this study. Note that due to the different function used for density dependence, the G_0 values of expressions (31) and (32) are not directly comparable.

$$G_{max} = G_0 p_{at} e^{-1.8} \left(\frac{p'}{p_{at}} \right)^{0.5} \quad \text{where} \quad G_0 = 530 \quad (32)$$

The value of G_{max} captured by small-strain measurements has been observed to be 2–4 times higher than that required to adequately model

the initial stages of monotonic shearing with bounding surface plasticity models (Papadimitriou et al., 2001; Andrianopoulos et al., 2010; Papadimitriou et al., 2023). Taiebat and Dafalias (2008) estimated the value of the small-strain shear modulus coefficient G_0 when calibrating SANISAND 2008 (Eq. (6)), by using the initial stages of stress–strain curves from drained monotonic compression tests (selecting the secant modulus at strain levels $\sim 3 \times 10^{-4}$, from observation). A similar approach was followed here as it yielded improved results in terms of capturing the modelled monotonic experiments. Along with the monotonic tests described in Section 4.1.2, slopes corresponding to G_0 , $G_0/2$ and $G_0/3$ of Eq. (32) are shown in Fig. 8. It was found that the average secant modulus at strain levels $\sim 3 \times 10^{-4}$ is $G_0/3$. The following expression was thus used for the shear modulus:

$$G = G_0 p_{at} e^{-1.8} \left(\frac{p'}{p_{at}} \right)^{0.5} \quad \text{where} \quad G_0 = 176.67 \quad (33)$$

Taiebat and Dafalias (2008) propose that the elastic bulk modulus, K (Eq. (7)) is to be obtained from isotropic unloading data. Eq. (34) is proposed for the incremental bulk modulus in isotropic unloading from triaxial experiments conducted in the University of Oxford on Hostun HN31 sand (Grey and Adamidis, 2024).

$$K = K_0 p_{at} e^{-2} \left(\frac{p'}{p_{at}} \right)^{0.65} \quad \text{where} \quad K_0 = 225 \quad (34)$$

4.3. Critical state parameter

The critical state line was described in Section 4.1.2. The state parameter definition by Been and Jefferies (1985) was used for this initial calibration, as noted in Eq. (5). The stress ratio η at critical state in triaxial compression, M_{cs} was determined as shown in Fig. 9. An $M_{cs} = 1.251$ yields a critical state friction angle $\phi_{cs} = 31.2^\circ$, which is very close to $\phi_{cs} = 31.5^\circ$ concluded by Azeiteiro et al. (2017). The value of m was chosen as 0.05 (Taiebat and Dafalias, 2008), which resolves the back-stress ratio at critical state, $\alpha^c = 1.201$, following Eq. (1). The critical state stress ratio in extension to that of compression was taken as $c = 0.71$ based on results presented by Azeiteiro et al. (2017). This yields a critical state friction angle $\phi_{cs} = 22.8^\circ$ in extension.

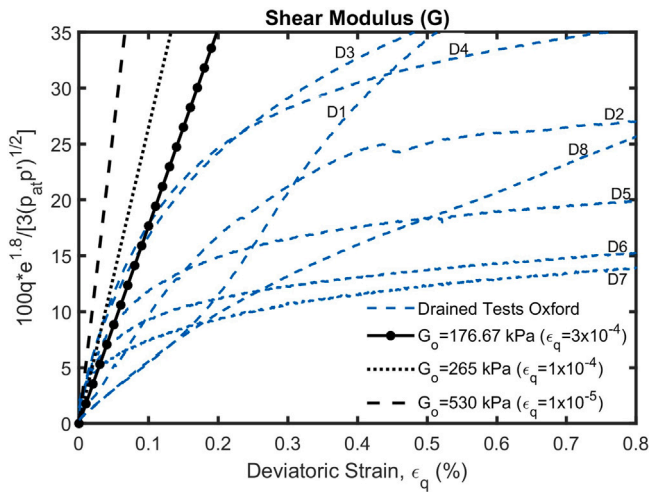


Fig. 8. Calibration of G_0 using data of drained triaxial compression tests on isotropically consolidated Hostun sand.

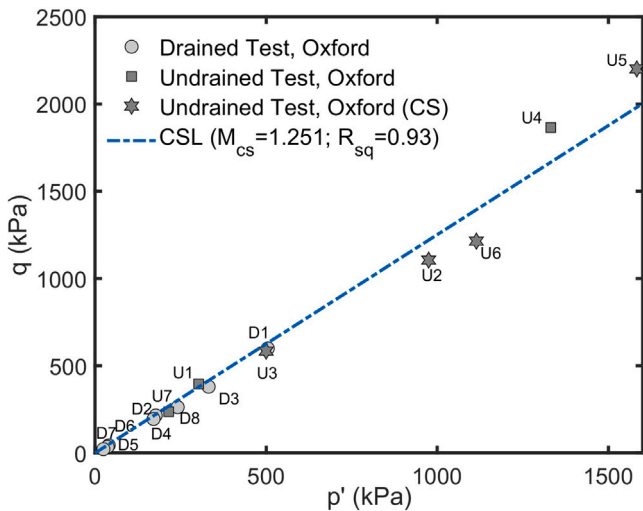


Fig. 9. Critical state strength of Hostun sand in compression.

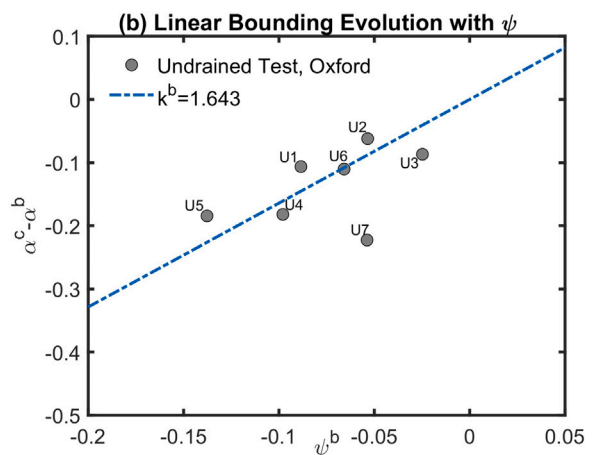
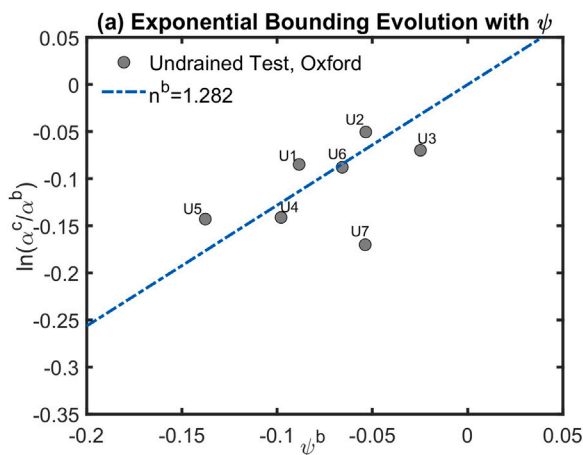


Fig. 10. Calibration of constants (a) n^b and (b) k^b (Eq. (2)) for Hostun sand using the results of undrained monotonic compression tests.

4.4. Bounding surface parameter

The bounding surface parameter, n^b was obtained from Eq. (2). The bounding surface, α^b was obtained from peak stress ratio states (PSRS), $\eta_{PSRS} - m$ from drained and undrained tests using Eq. (1). For an exponential bounding evolution, $\ln(\alpha^c/\alpha^b)$ and for a linear bounding evolution, $(\alpha^c - \alpha^b)$ were plotted against the corresponding state parameter, ψ . The slope of the fitted line gives the n^b and k^b values, as shown in Figs. 10(a) and 10(b), respectively. Undrained tests were prioritised in calibration, since as volume controlled they are closer to the coupled strain tests that we aim to simulate.

4.5. Dilatancy surface parameter

The dilatancy surface parameter, n^d was selected based on Eq. (3). The dilatancy surface, α^d was obtained from the stress ratio at phase transformation state (PTS), so that $\alpha^d = \eta_{PTS} - m$ from undrained tests. For an exponential evolution, $\ln(\alpha^d/\alpha^c)$ and for a linear evolution, $(\alpha^d - \alpha^c)$ were plotted against the corresponding state parameter, ψ . The slope of the fitted line gives the n^d and k^d value, respectively (Figs. 11(a) and 11(b)).

4.6. Stress-dilatancy characteristics

The dilatancy parameter, A_d was determined from stress-dilatancy curves obtained from drained tests using Eq. (14), where the dilatancy parameter D is expressed as a function of the difference between the slope of the dilatancy surface, α^d and the current stress ratio α . The dilatancy D is a ratio of the plastic volumetric to the plastic deviatoric strain increment (Eq. (11)), so that $D = \epsilon_v^p / \epsilon_q^p$ for monotonic compression tests, where $\epsilon_q^p > 0$. In order to obtain plastic strain increments, the elastic strain increments must be subtracted from the total strain increments. The elastic strain increments can be computed based on Eqs. (9) and (10), where the tangent elastic moduli are taken from Eqs. (33) and (34). This approach has been used before by Azeiteiro et al. (2017) for drained tests. The data was plotted for axial strains ranging from 1% to peak stress ratio in Fig. 12. The slope of the stress-dilatancy curves gives the A_d value.

Taiebat et al. (2010) estimated the A_0 parameter in SANISAND 2004 (Dafalias and Manzari, 2004) by plotting the deviatoric stress, q against void ratio, e from drained experiments and taking the value of A_0 that gives the best-fit simulation, following a trial and error approach. A similar process, depicted in Fig. 13, verifies that the value of $A_d = 1$ from Fig. 12 is appropriate.

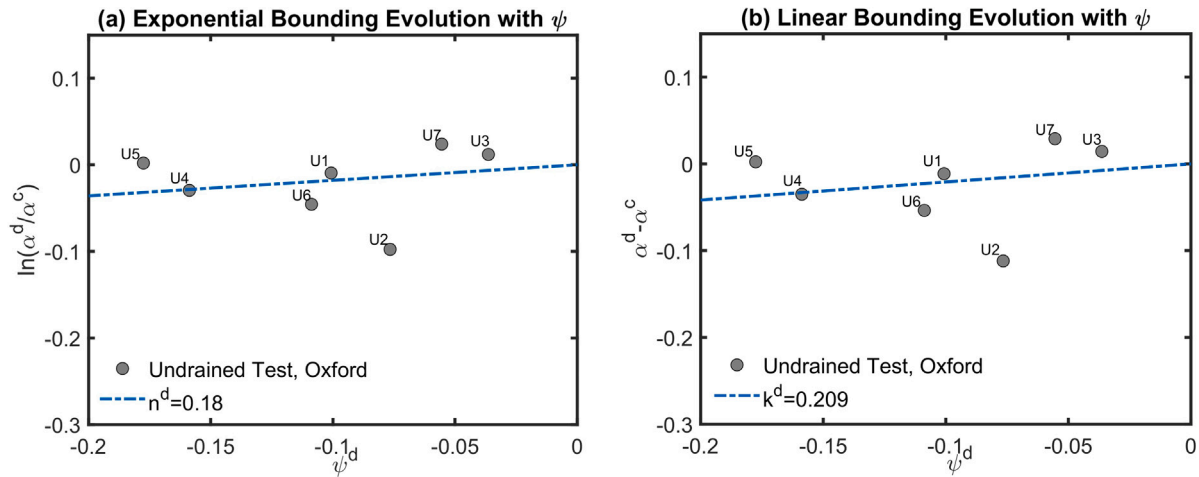


Fig. 11. Calibration of constants (a) n^d and (b) k^d (Eq. (3)) for Hostun sand using the results of undrained monotonic compression tests.

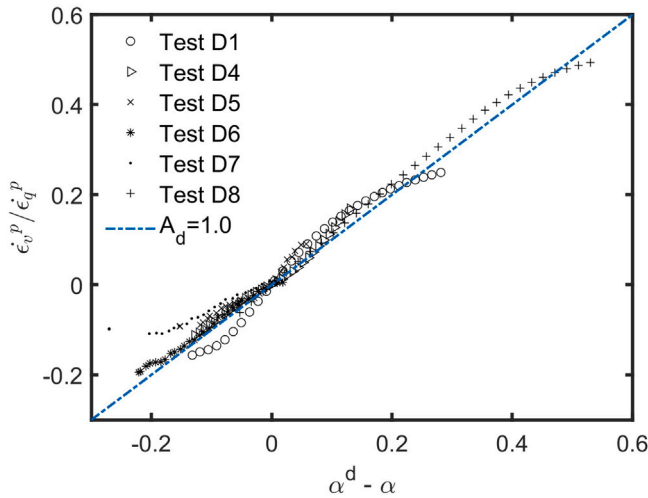


Fig. 12. Calibration of constant A_d (Eq. (14)) for Hostun sand using the results of drained monotonic compression tests.

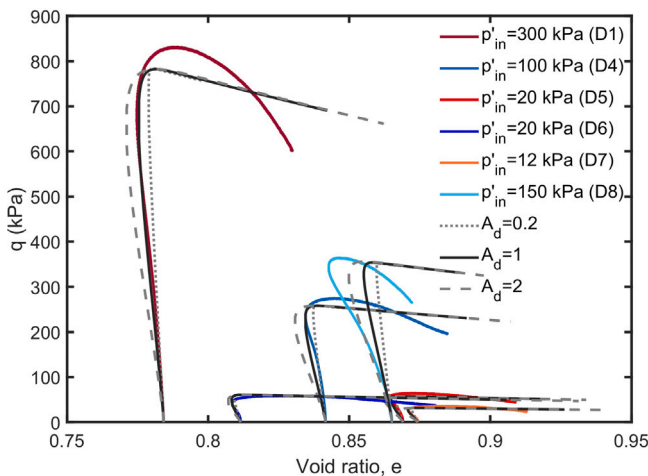


Fig. 13. Calibration of dilatancy parameter A_d using drained monotonic triaxial tests on Hostun sand.

4.7. Bounding parameters h_0 and c_h

The bounding parameters h_0 and c_h pertain to the distance from the bounding surface and according to Taiebat and Dafalias (2008) are to be determined using trial and error. The undrained test data were used to calibrate these parameters by fitting simulation results to the experimental curves of deviatoric stress, q versus axial strain, ϵ_1 , varying the function of h_0 and c_h in Eq. (13), and aiming to capture the response at low strains, as in Taiebat et al. (2010). The exponential function of h_0 and c_h as noted in Section 2.1 provided a better overall fit for all tests. Fig. 14 shows this calibration process, including two examples of undrained tests.

4.8. Compression parameters

The compression parameters are applicable for loading at high-confining pressures related to the limiting compression curve regime, which is around $p' = 10 - 50$ MPa for siliceous sands (Taiebat and Dafalias, 2008). Liquefaction related studies are conducted at low confining pressure range as the phenomenon involves a gradual reduction in effective confining stress to failure. Particle crushing does not contribute significantly to the plastic strains and strength characteristics in liquefaction triggering, which is why the compression properties of Hostun sand were not probed in this study, as in other liquefaction studies (e.g. Taiebat et al., 2010; Kassas et al., 2021; Andrianopoulos et al., 2010; Yang et al., 2022; Petalas et al., 2019). In fact, the model used here (Taiebat and Dafalias, 2008) is an exception within the SANISAND family, whose models generally do not allow for consideration of the compression property. Nevertheless, the compression property could further improve simulation of stress-strain behaviour at higher stresses (Taiebat et al., 2010), especially for crushable sands, such as calcareous sands (McDowell and Bolton, 1998).

4.9. Model performance

A summary of the calibrated model parameters are listed in Table 5. p_{at} is taken as 100 kPa. Some characteristic simulations of the experimental tests are presented in this section. The model was found to perform in a similar way under either a linear (Eq. (2)) or an exponential (Eq. (3)) evolution assumption of the bounding and dilatancy surfaces with the state parameter. Here, a linear evolution was used, as it was found to be advantageous for the partially drained investigation presented in the next section.

Fig. 15 shows a comparison between the numerical simulations and the experimental data for undrained tests, while Fig. 16 shows a comparison for drained tests. The numerical simulations are able

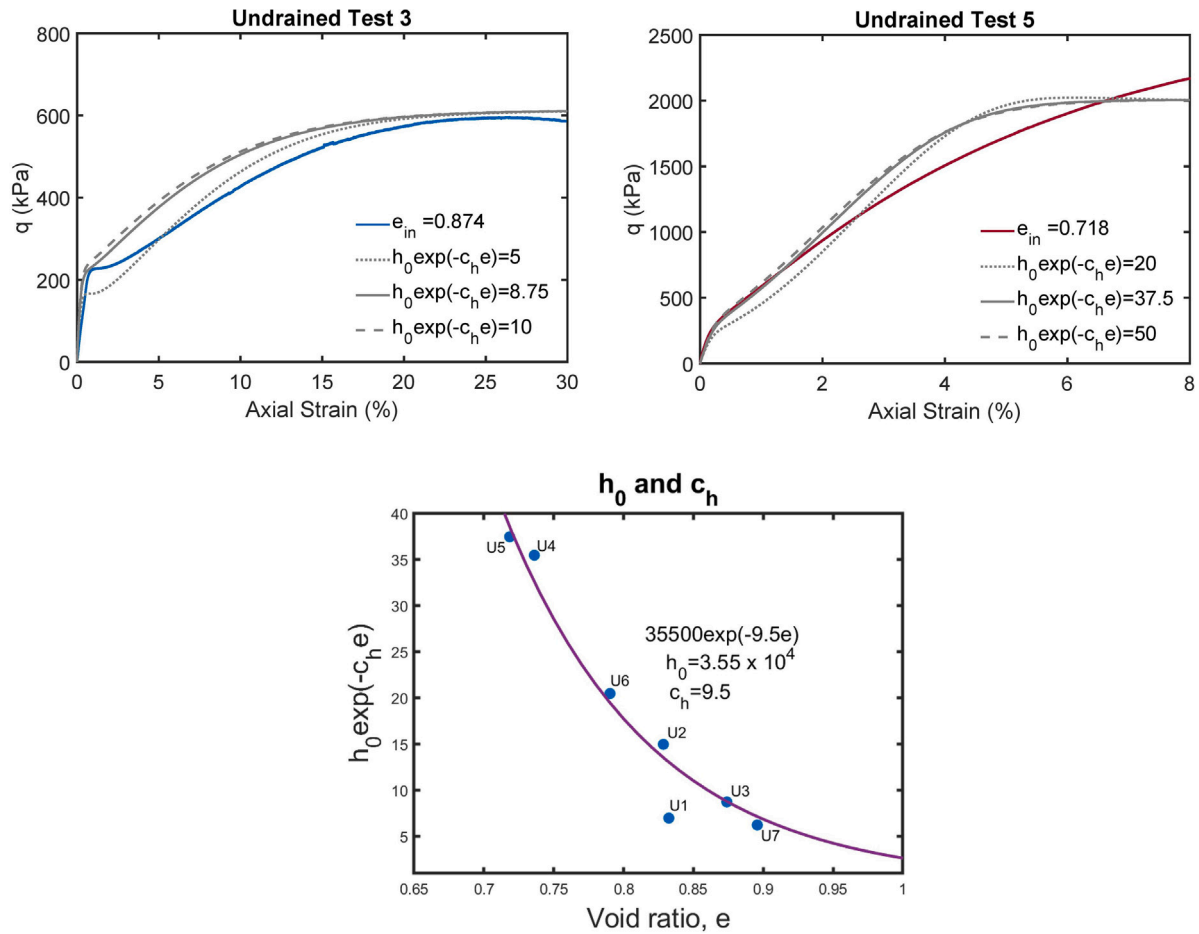


Fig. 14. Calibration of h_0 and c_h for Hostun sand using the results of undrained monotonic compression tests.

Table 5

SANISAND model parameters for Hostun sand, refer Section 2.1 for other parameter definitions.

Parameter	Parameter	Parameter	Parameter
G_0 (kPa)	176.67 ^a	e_{max}	0.993
K_0 (kPa)	225 ^b	e_{min}	0.647
α^c	1.201	R	0.73
c	0.71	Q	8.3
		n^b	1.282
		k^b	1.643
		h_0	3.55×10^4
		c_h	9.5 ^c
		A_d	1
		m	0.05

^a Implemented in Eq. (33).

^b Implemented in Eq. (34).

^c Exponential function used, see Section 4.7.

to capture the behaviour sufficiently well across a range of densities. The same calibration parameters are used to predict partially drained experiments in the following section.

5. Partially drained behaviour of Hostun sand

The partially drained behaviour of Hostun sand was experimentally examined by conducting coupled strain triaxial compression tests, imposing an axial strain of up to 35% at a rate of 6 mm/hr and a volumetric strain rate that was a percentage of the axial strain rate. The testing methodology is the same as discussed for the drained/undrained monotonic compression tests in Section 4.1.

5.1. Partially drained experimental test results

Table 6 summarises the initial states and results of the partially drained monotonic triaxial compression experiments. Three constant

ratios of volumetric strain rate to axial strain rate, $\zeta = \dot{\epsilon}_v/\dot{\epsilon}_1$ were used. The LCSi points, as discussed in Section 3, were identified by imposing Eq. (20) to the experimental data and selecting points post-phase transformation and post-peak stress ratio states. The LCSi points obtained in Table 6 occur post-phase transformation states and post-peak stress ratio states. Thus, they satisfy both Condition 1 (Eq. (28)) and Condition 2 (Eq. (29)) required to isolate a single state parameter. Unlike for the undrained tests, the phase transformation point cannot be accurately determined for partially drained tests as $p' \neq 0$ at phase transformation state.

All experimental results, along with simulations are shown in $e - p'$ space in Fig. 20 in Section 5.2.

5.2. Partially drained simulation results

Using the calibration parameters from Table 5 and a linear evolution of bounding surfaces, the partially drained triaxial tests of Section 5.1 were numerically simulated in SANISAND 2008 (Taiebat and Dafalias, 2008) by imposing a volumetric strain rate as a function of the imposed axial strain rate. Figs. 17–19 show the comparison of experimental and numerical results for each coupling ratio at the highest and lowest densities obtained during testing. The instability points are shown in square markers for the simulation and star markers for the experimental data. The comparison reveals that the calibration performs better for the denser specimens across all strain coupling ratios, ζ . For the looser specimens, the comparison is poor. The simulated stress paths in $q - p'$ space only capture the experimental response before dilation commences. The peak deviator stresses predicted are much higher than the observed ones. Across all densities, the instability point is detected

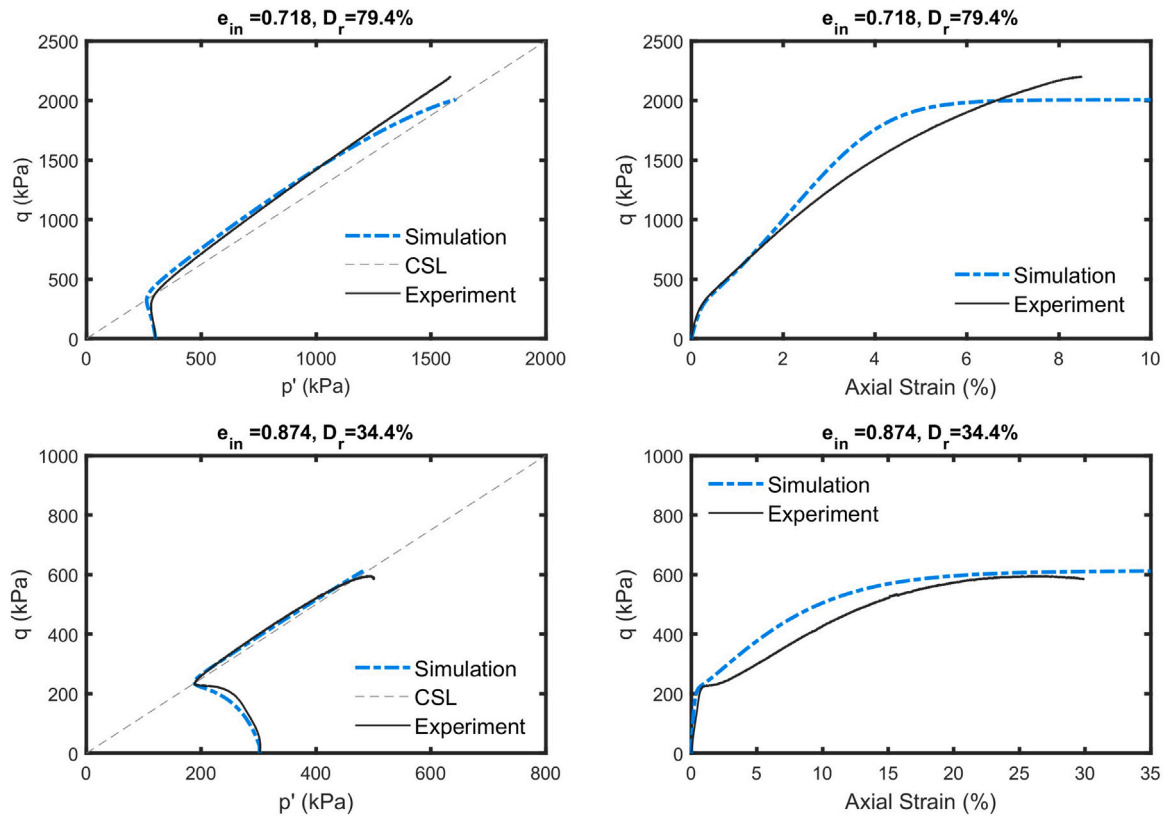


Fig. 15. Simulations of undrained monotonic triaxial compression tests on isotropically consolidated samples of Hostun sand and comparison with experimental test data (top-bottom: Tests U5 and U3).

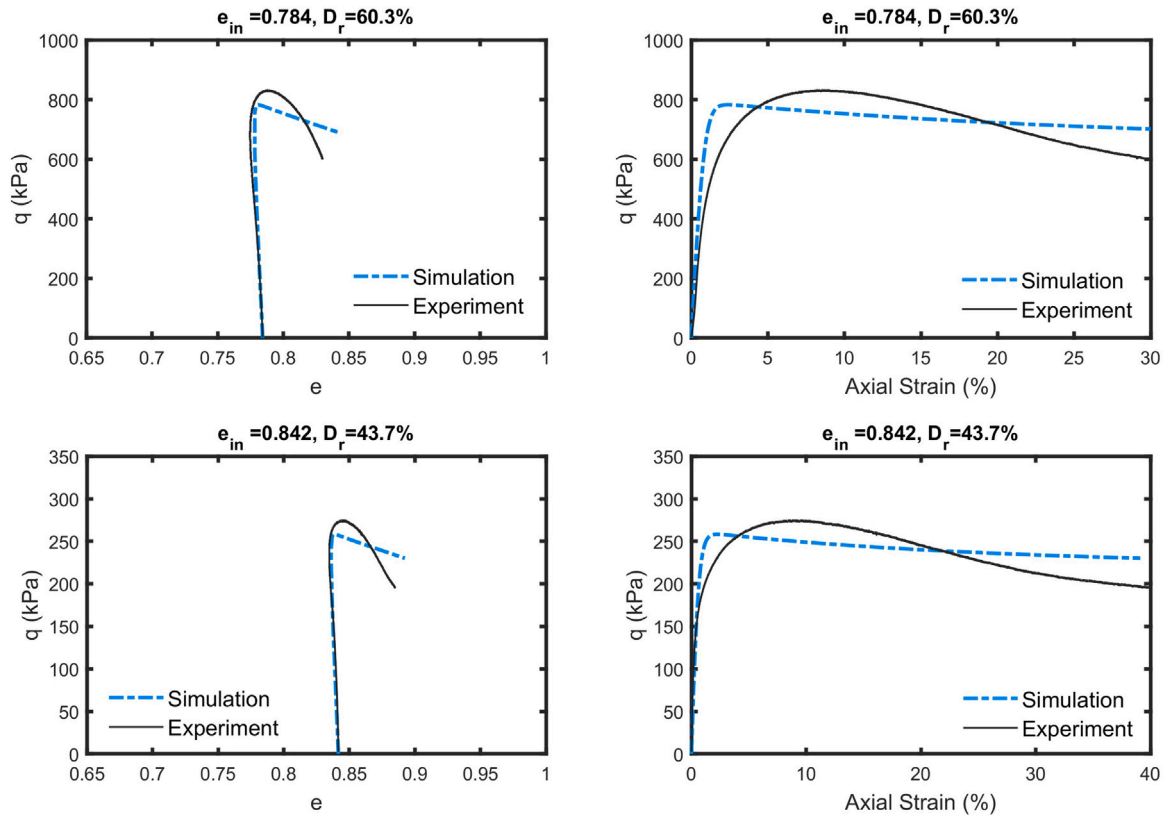


Fig. 16. Simulations of drained monotonic triaxial compression tests on isotropically consolidated samples of Hostun sand and comparison with experimental test data (top-bottom: Tests D1 and D4).

Table 6Results of partially drained monotonic triaxial tests performed under three different values of $\zeta (= \epsilon_v/\epsilon_1)$.

Test	ID ^a	e_{in} ^b	p'_{in} ^b	e_{INST} ^c	p'_{INST} ^c	η_{PSRS} ^d	ϕ_{PSRS} ^d	η_{end} ^e	ϕ_{end} ^e
ICPDMC/0.758/300/-5 (P1)		0.758	300	0.774	963.9	1.40	34.5°	1.16	29.2°
ICPDMC/0.800/100/-5 (P2)		0.800	100	0.819	459	1.39	34.4°	1.17	29.2°
ICPDMC/0.825/60/-5 (P3)		0.825	60	0.846	297	1.42	35.1°	1.14	28.7°
ICPDMC/0.842/20/-5 (P4)		0.842	20	0.861	191.4	1.42	35.0°	1.12	28.1°
ICPDMC/0.722/300/-10 (P5)		0.722	300	0.744	1015.9	1.44	35.4°	1.18	29.6°
ICPDMC/0.748/250/-10 (P6)		0.748	250	0.773	738.3	1.43	35.3°	1.18	29.5°
ICPDMC/0.818/80/-10 (P7)		0.818	80	0.840	105.7	1.39	34.5°	0.99	25.1°
ICPDMC/0.828/30/-10 (P8)		0.828	30	0.853	78.4	1.44	35.4°	1.01	25.6°
ICPDMC/0.714/300/-15 (P9)		0.714	300	0.742	927.6	1.48	36.4°	1.19	29.8°
ICPDMC/0.737/250/-15 (P10)		0.737	250	0.768	635.7	1.46	35.9°	1.17	29.2°
ICPDMC/0.763/100/-15 (P11)		0.763	100	0.793	385.4	1.45	35.8°	1.12	28.1°
ICPDMC/0.804/50/-15 (P12)		0.804	50	0.829	81.2	1.41	34.9°	0.52	13.8°

^a (1) type of consolidation: IC or K0 for isotropic or anisotropic consolidation, respectively; (2) type of drainage: D for drained, U for undrained and PD for partially drained; (3) type of loading: MC or ME for monotonic compression or monotonic extension; (4) void ratio immediately after consolidation; (5) mean effective stress immediately after consolidation; and (6) coupled strain ratio at shearing stage, $\zeta = \epsilon_v/\epsilon_1$ in percentage.

^b Post consolidation values;

^c INST: Instability Point;

^d PSRS: Peak stress ratio state;

^e End of test.

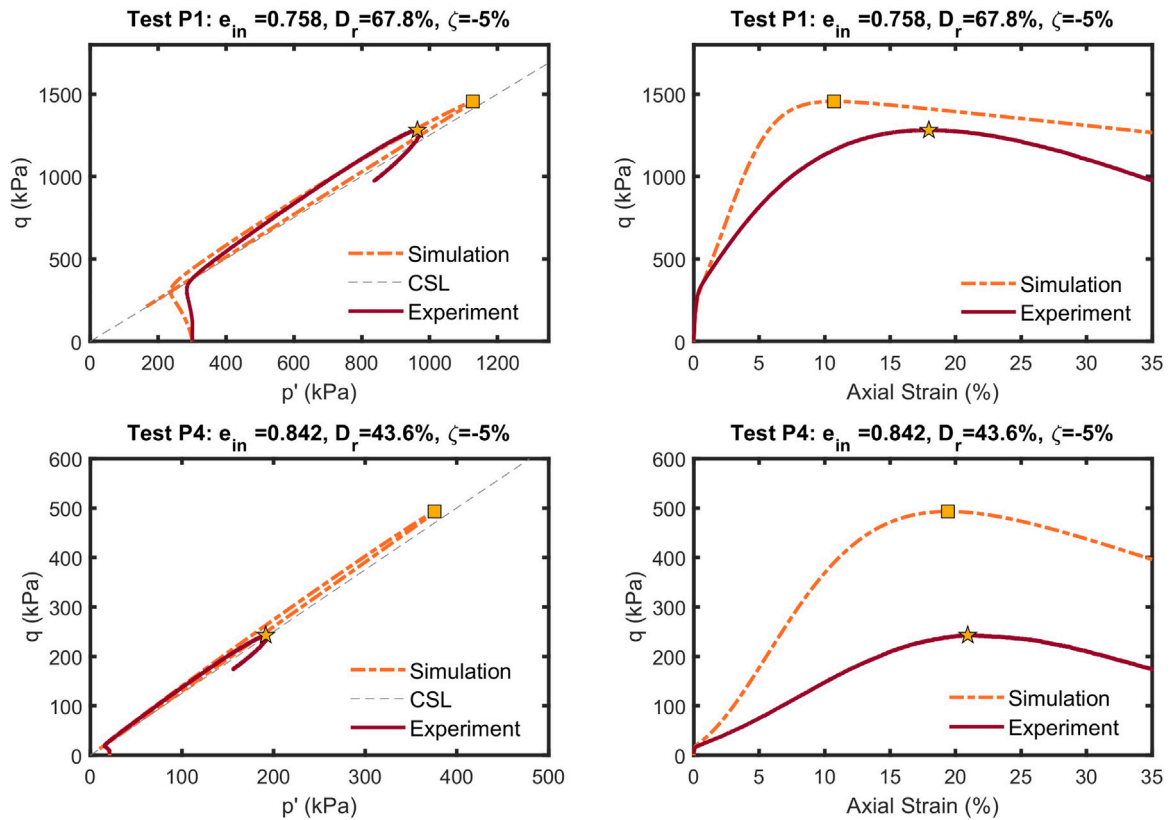


Fig. 17. Simulations of partially drained monotonic triaxial compression tests under $\zeta = -5\%$ on isotropically consolidated samples of Hostun sand and comparison with experimental test data.

at axial strains close to the observed values. Given that the performance of the model in simulating partially drained behaviour notably varies with the initial density, the results are plotted in $e - p'$ space in Fig. 20 and compared against the experimental data.

Constant ψ lines were plotted as dotted lines in Fig. 20, using Eq. (27), and are shown to represent well the locus of the numerically obtained instability points (numerical LCS curve). However, the experimental LCS points do not fall on the same curve. As the stress paths of the densest specimens (Tests P1, P5 and P9) are captured better by the constitutive model under coupled strain ratios, a constant ψ curve

is drawn through each of the densest experimental instability points, represented in a dashed line in Fig. 20. It is evident that the LCS points from the remaining 3 experiments for each coupling strain ratio do not fall on the same constant ψ curve. However, since LCS points under the same strain coupling ratio must satisfy the condition of a constant ψ (Eq. (27)) when modelled with the selected SANISAND model (Taiebat and Dafalias, 2008), the definition of the state parameter, ψ , must be updated so that a constant ψ curve coincides with the experimentally observed LCS for the used constitutive model.

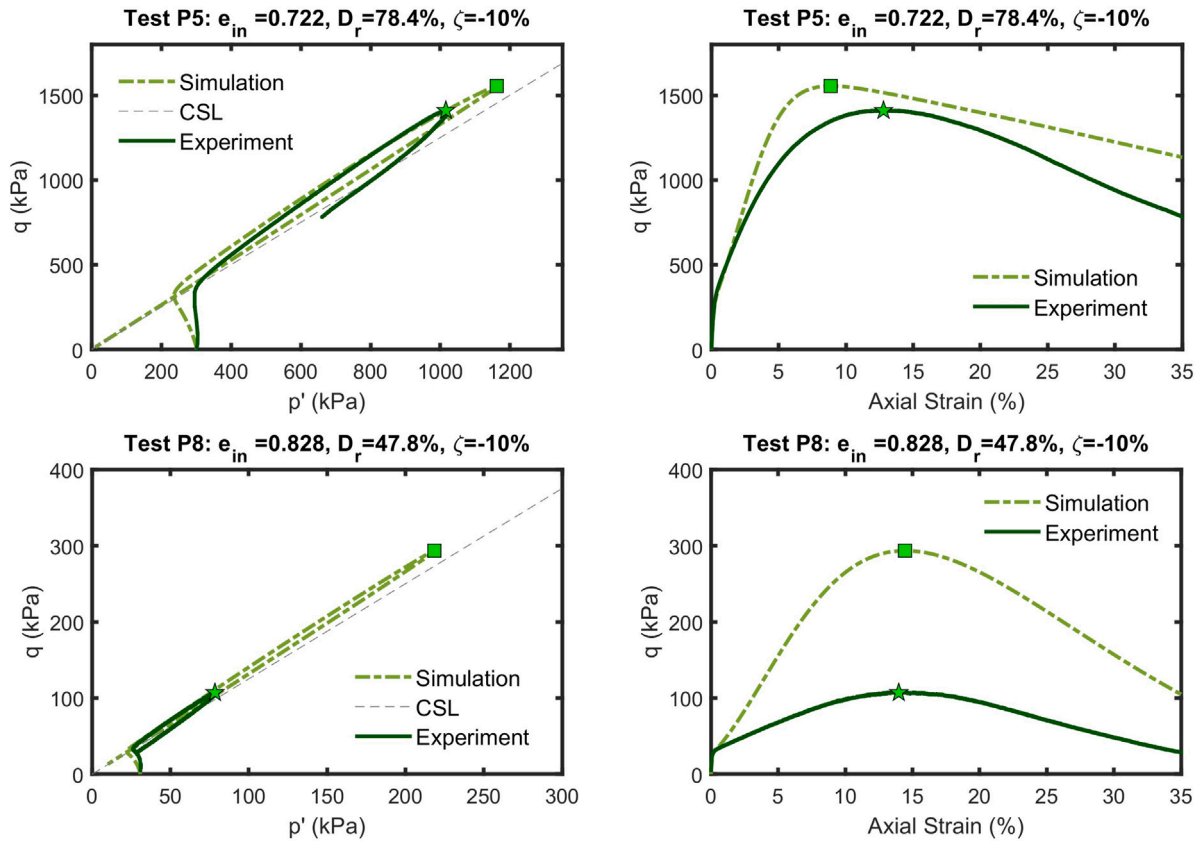


Fig. 18. Simulations of partially drained monotonic triaxial compression tests under $\zeta = -10\%$ on isotropically consolidated samples of Hostun sand and comparison with experimental test data.

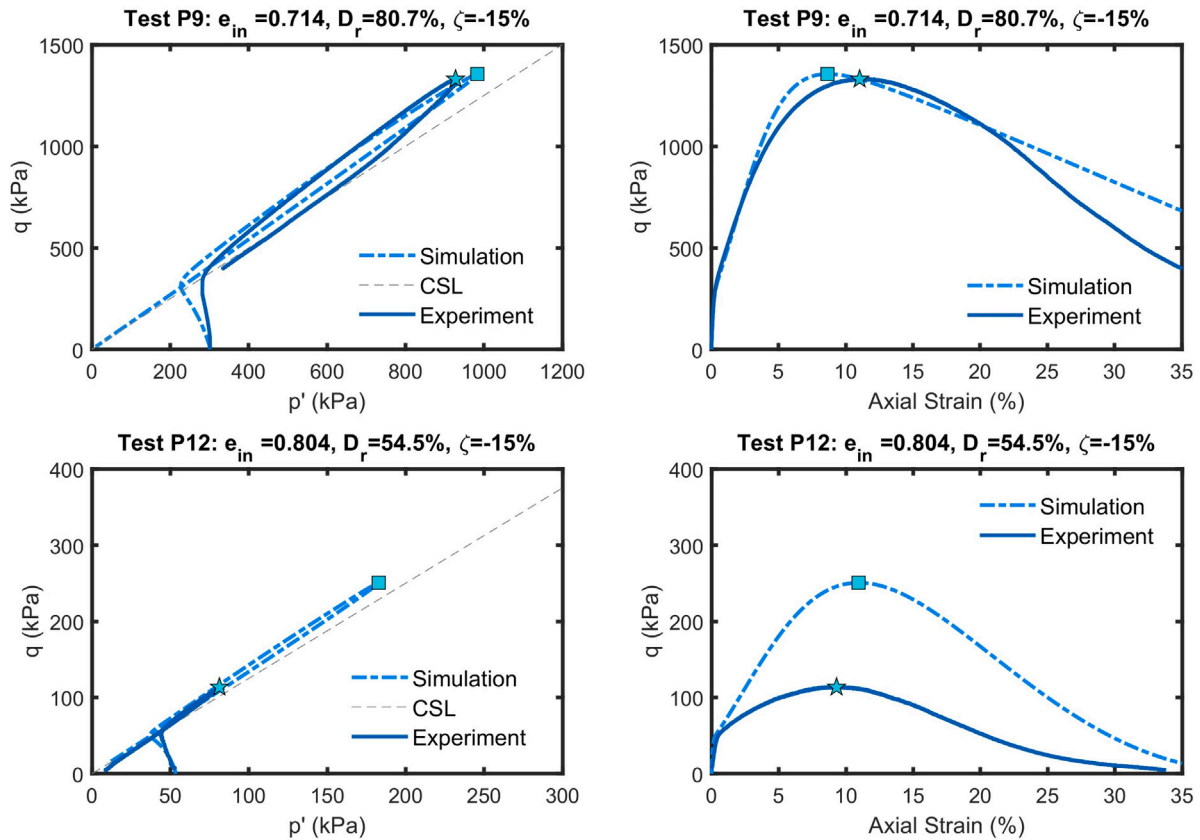


Fig. 19. Simulations of partially drained monotonic triaxial compression tests under $\zeta = -15\%$ on isotropically consolidated samples of Hostun sand and comparison with experimental test data.

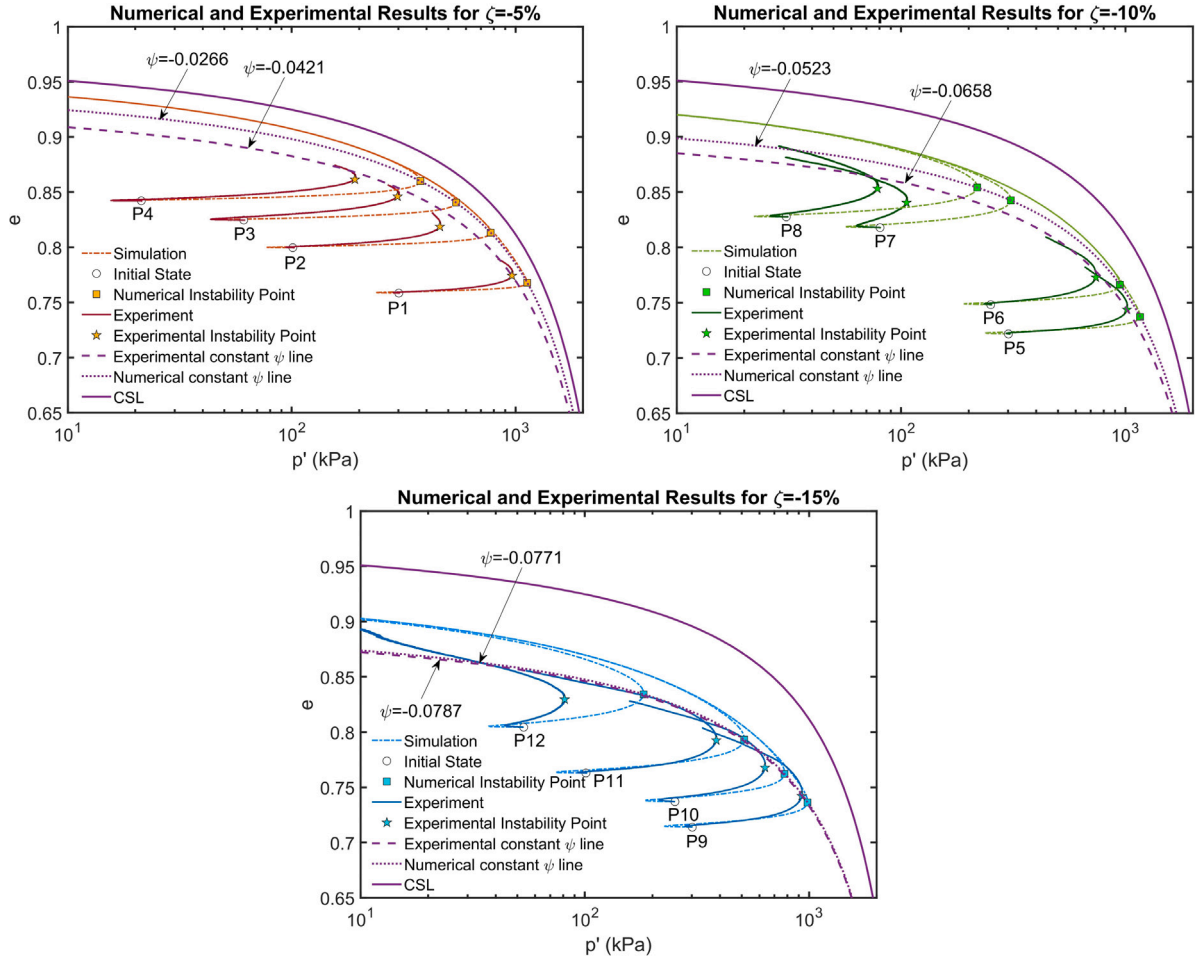


Fig. 20. Simulations of partially drained monotonic triaxial compression tests under $\zeta = -5\%$, -10% and -15% in $e - p'$ space and comparison with experimental test data.

5.3. Updated state parameter definition

Updated state parameter definitions proposed in literature (Verdugo, 1992; Ishihara, 1993; Wang et al., 2002; Dafalias and Manzari, 2004) such as the state index $I_s = (e_0 - e)/(e_0 - e_{cs})$, pressure index $I_p = p'/p'_{cs}$, horizontal distance $p' - p'_{cs}$ and e/e_{cs} were explored to obtain a better fit to the experimental points. The best fit to the experimentally obtained LCSIs was obtained for the e/e_{cs} index, across all strain coupling ratios $\zeta (= \epsilon'_v/\epsilon'_1)$, as seen in Fig. 21. Nevertheless, the e/e_{cs} index does not maintain the practicality of a state parameter value of zero at the CSL, a negative value for states below the CSL and a positive value for states above the CSL, which is important for the way the equations of SANISAND 2008 (Taiebat and Dafalias, 2008) are cast. To amend this issue, a function of the natural logarithm of e/e_{cs} can be used as an updated state parameter ψ_D . A general form that satisfies the above considerations is proposed in Eq. (35), with x and w as fitting parameters. For a constant updated state parameter ψ_D , the vertical distance from the CSL is reduced as p' increases.

$$\psi_D = x \cdot \text{sign}[\ln(\frac{e}{e_{cs}})] |\ln(\frac{e}{e_{cs}})|^w \quad (35)$$

The parameters x and w in Eq. (35) must be chosen so that Eq. (27) is satisfied at the LCSIs points under each strain coupling ratio ζ . The benefit of a linear bounding surface evolution over an exponential evolution definition (Eqs. (2) and (3)) is that by using it, one can analytically solve Eq. (27) for ψ , given the ζ and relevant model constants appearing in the equation. Parameter k^b of Eq. (27) is determined from Eq. (36), following Eq. (2), at the peak stress ratio state (PSRS) and parameter k^d is determined from Eq. (37), following Eq. (3), at the

phase transformation state (PTS) in undrained monotonic compression tests. The denominators of Eqs. (36) and (37) include the coefficient x of Eq. (35). In Eq. (27), $(k^b + k^d)$ is multiplied by the ψ_D value at the LCSIs points, which also includes the coefficient x . Since parameter x appears in both the numerator and denominator of Eq. (27), its value is inconsequential and x can be taken as equal to 1, for the sake of simplicity.

$$k^b = \frac{\alpha^c - \alpha_{PSRS}}{\psi_{D,PSRS}} \quad (36)$$

$$k^d = \frac{\alpha_{PTS} - \alpha^c}{\psi_{D,PTS}} \quad (37)$$

It is shown from Eqs. (36) and (37) that k^b and k^d are dependent on the state parameter definition, and thereby depend on the parameter w . The numerators of Eqs. (36) and (37) remain constant. Parameter A_d was obtained from drained monotonic compression tests using Eq. (14), which can be expanded using the definition of dilatancy D and Eq. (37) and expressed as Eq. (38). The left-hand side of Eq. (38) is derived from the experimental data and is independent of the state parameter definition chosen. The right-hand side is a function of the ratio $\psi_D/\psi_{D,PTS}$ and thus dependent on parameter w . The other parameters included in the right-hand side are derived directly from experimental data and remain unaffected by w .

$$\frac{\epsilon'_{v,p}}{\epsilon'_{q,p}} = A_d(\alpha^c + (\frac{\alpha_{PTS} - \alpha^c}{\psi_{D,PTS}})\psi_D - \alpha) \quad (38)$$

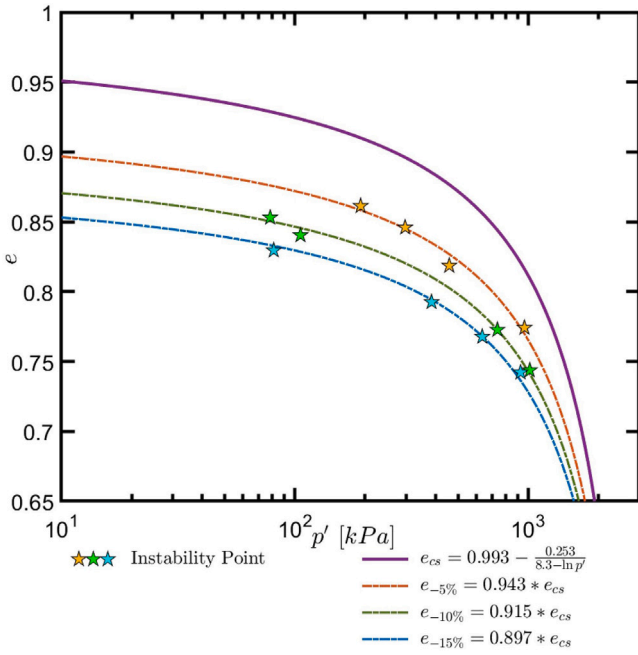


Fig. 21. Experimental instability points from partially drained monotonic triaxial tests under strain coupling ratio, $\zeta = -5\%$, -10% and -15% and corresponding constant state parameter instability lines.

As all parameters on the left-hand side of Eq. (27) are dependent on the state parameter definition chosen, which in this case depends on parameter w , a range of values were examined to determine the exponent w , ranging between 0.2 and 4. Parameters k^b , k^d and A_d corresponding to the new exponent were determined for each value of w through the calibration procedure discussed in Section 4. These parameters along with the constant state parameter value ψ_D corresponding to the LCSi at each strain coupling ratio ζ were then used to calculate the left-hand side of Eq. (27). The result was compared to the right-hand side of Eq. (27) and the coefficient of determination (R^2) was computed, across all strain coupling ratios examined. The value of w corresponding to the maximum R^2 was taken as the overall best-fit value for the exponent. The outcome of this process is shown in Fig. 22. The calibrated values of k^b and k^d with each variation of exponent w

are shown in Fig. 23. The parameter A_d is shown in Fig. 24 at each value of exponent w . The variation in A_d with w is insignificant, and thus the initially obtained value can be maintained across iterations.

In Fig. 22, a maximum overall R^2 value is attained at $w = 1.6$. The updated state parameter for Hostun HN31 sand can thus be fully defined by Eq. (39). This updated state parameter function should be able to capture the locus of the experimentally observed constant state instability points (LCSi) using the SANISAND 2008 model, as derived in Eq. (27).

$$\psi_D = \text{sign}[\ln(\frac{e}{e_{cs}})] |\ln(\frac{e}{e_{cs}})|^{1.6} \quad (39)$$

From the monotonically increasing values of k^b and k^d with w (Fig. 23), as well as from the results of Fig. 22, one can observe that an iterative procedure for the determination of w would converge. Fig. 25 shows the results from an iterative procedure of determining the exponent w . For each iteration, k^b and k^d values were obtained from calibration using the state parameter definition of Eq. (35) with $x = 1$, with a starting value of $w = 1$. These k^b and k^d values were incorporated in Eq. (27) and the equation was solved at each strain coupling ratio for a new best-fit value of the state parameter exponent w_i , to be used for the i th iteration. This process was repeated until w , k^b and k^d converged. The values converged within 1% after 15 iterations. Thus, an iterative procedure, as illustrated in Fig. 26, is recommended to determine the exponent in a computationally efficient manner.

5.4. Model calibration with updated state parameter

In this section, the model parameters for the SANISAND 2008 model are presented, corresponding to the updated state parameter definition given in Eq. (39). Note that the elastic moduli and critical state parameters remain unchanged as they do not have a dependence on the state parameter and are directly obtained from experimental data. The calibration of bounding parameter k^b and dilatancy parameter k^d for $w = 1.6$ is determined in Fig. 23. Parameter A_d was shown to remain unchanged in Fig. 24. Finally, the bounding parameters h_0 and c_h were calibrated, as described in Section 4.7, and were also found to closely match the values determined with the original definition (Eq. (5)). Table 7 summarises the model parameters corresponding to the updated state parameter ψ_D (Eq. (39)).

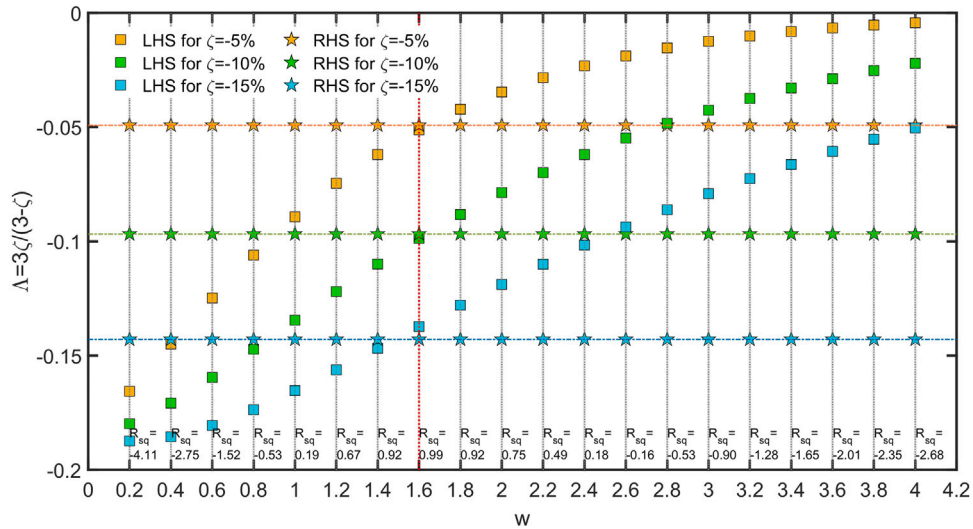


Fig. 22. Variation of left-hand side (LHS) of Eq. (27) with exponent w using updated state parameter definition ψ_D (Eq. (35), where $x = 1$) and comparison with right-hand side (RHS) for convergence.

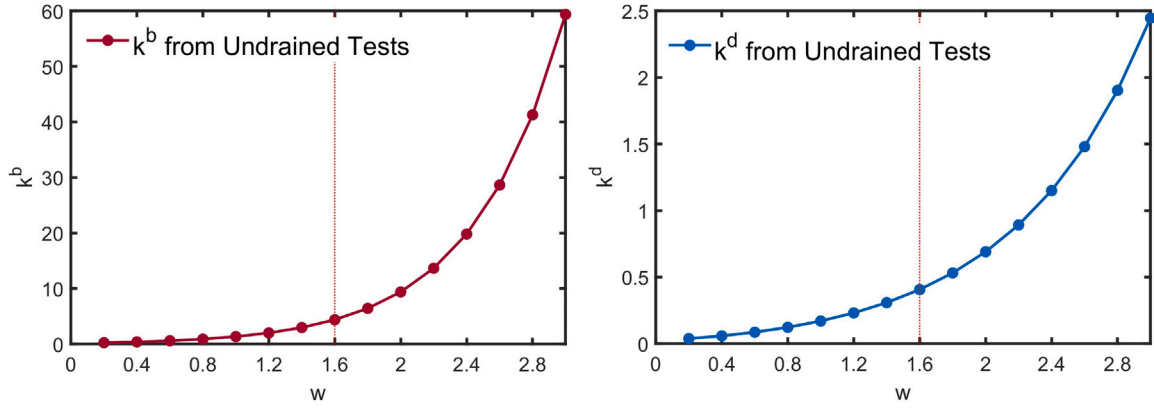


Fig. 23. Calibration of constants k^b (Eq. (2)) and k^d (Eq. (3)) for Hostun sand with updated state parameter definition ψ_D (Eq. (35), where $x = 1$).

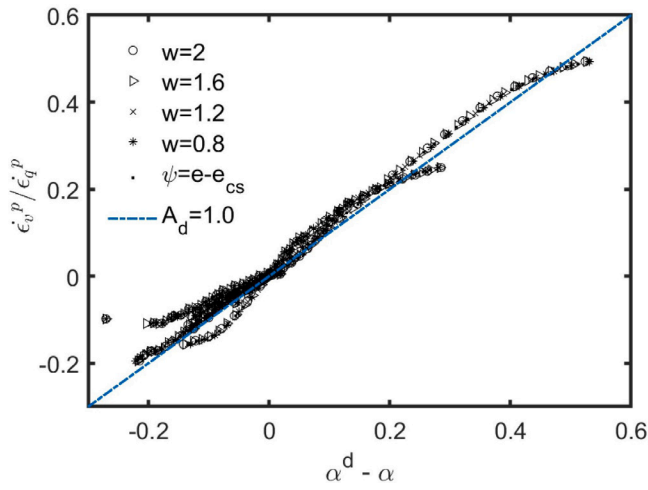


Fig. 24. Calibration of constants A^d (Eq. (14)) for Hostun sand with updated state parameter definition ψ_D (Eq. (35), where $x = 1$).

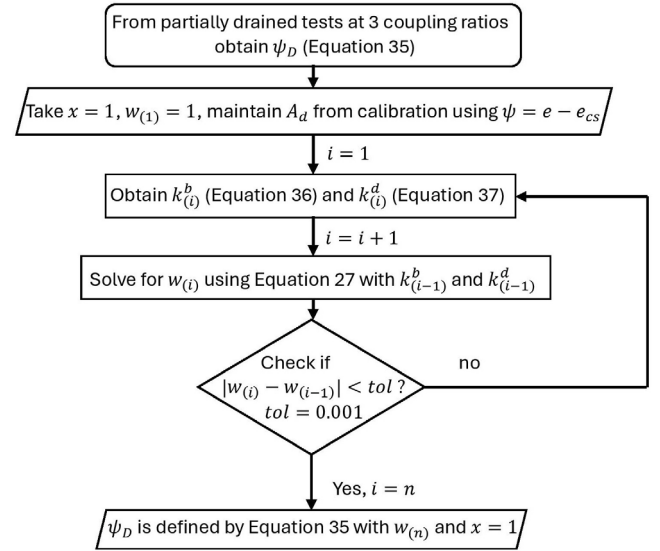


Fig. 26. Flowchart showing steps to determine updated state parameter function, ψ_D .

Table 7

SANISAND model parameters for Hostun sand with the updated state parameter definition ψ_D (Eq. (39)), refer Section 4.9 for other parameter definitions.

Parameter		Parameter		Parameter	
k^b	4.39	k^d	0.407	A_d	1
h_0	3.55×10^{4a}	c_h	9.5^a		

^a Exponential function used, see Section 4.7.

6. Model performance with updated state parameter

Using the calibrated model parameters listed in Table 5 and Table 7, the experimental tests were numerically simulated. The simulation results of undrained, drained and partially drained monotonic compression tests are presented in this section.

6.1. Simulation of undrained and drained monotonic triaxial tests

Fig. 27 shows a comparison of the numerical simulation results and experimental data of undrained tests on Hostun sand while Fig. 28 shows a comparison for drained tests. In both figures, the numerical simulations with the updated state parameter definition adequately capture the experimentally observed behaviour. Comparing the undrained test simulations with those of Fig. 15, it is observed that

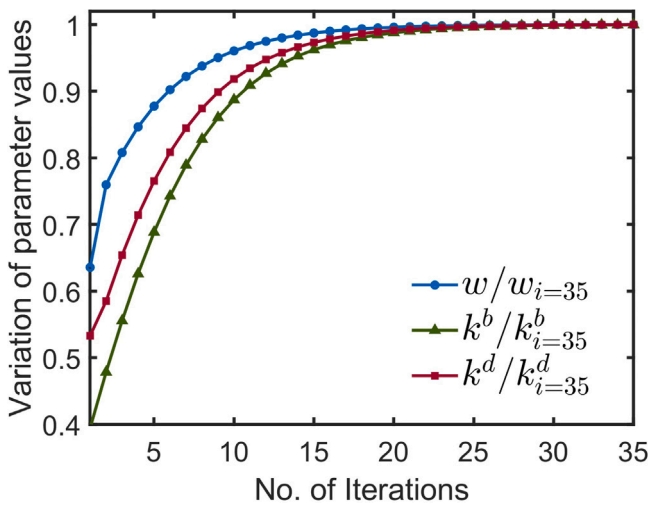


Fig. 25. Variation of parameter values with each iteration using updated state parameter definition ψ_D (Eq. (35), where $x = 1$).

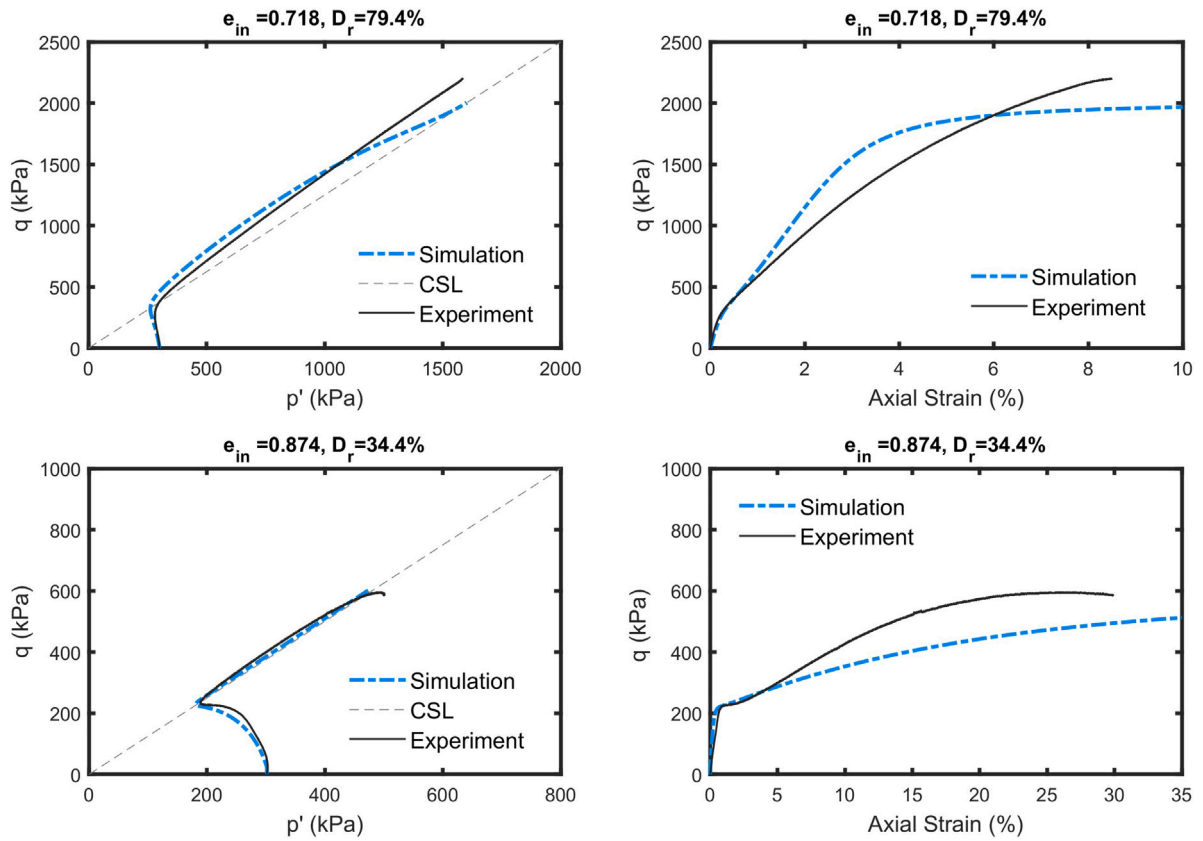


Fig. 27. Simulations of undrained monotonic triaxial compression tests on isotropically consolidated samples of Hostun sand using updated ψ_D (Eq. (39)) and comparison with experimental test data (top-bottom: Tests U5 and U3).

the critical state is attained at larger strains with the updated state parameter definition. This is because the state parameter value now is smaller in magnitude than with the original definition (Been and Jefferies, 1985), which indicates an increased proximity of the initial state to the CSL. As these specimens are dense of critical, with negative state parameter values, the bounding surface in stress space is lower with the updated state parameter ψ_D , resulting in a reduction of the hardening modulus H (Eq. (13)) and a slower progression towards the critical state. The maximum deviatoric stresses attained under both undrained and drained condition are slightly lower than the values obtained with the original state parameter definition, which is also because of the reduction in the bounding surface stress ratio (α^b). The simulated stress-strain path at higher stresses could be improved further by including the compression property parameter in the model.

6.2. Simulation of partially drained monotonic triaxial tests

The partially drained triaxial tests of Section 5.1 were numerically simulated in SANISAND 2008 using the updated state parameter definition ψ_D . Comparisons of the numerical and experimental data for each strain coupling ratio are shown in Figs. 29–31 at the initial states corresponding to highest and lowest densities obtained during testing. The LCSi points are shown in square markers for the simulation and star markers for the experimental data.

The comparison shows remarkable improvement in the performance of the model across all densities and strain coupling ratios, ζ . The peak deviatoric stresses predicted for the looser specimens under strain coupling ratios, $\zeta = -10\%$ and $\zeta = -15\%$, are now much closer to the experimentally observed, as compared to those obtained with the previous calibration using the original state parameter ψ definition (Eq. (5)). The instability points are detected at axial strains close to the observed values. Comparing the numerical simulation and experimental data in

$e - p'$ space, the experimental instability points forming the LCSi curve now fall on the numerically obtained LCSi, both at a constant updated state parameter ψ_D , as shown in dotted lines in Fig. 32.

These results confirm that the proposed updated state parameter definition, ψ_D (Eq. (39)), significantly improves the performance of the selected constitutive model for the partially drained, coupled strain experiments examined in this investigation. The locus of constant state parameter instability points obtained using Eq. (27) accurately represents all experimentally observed instability points. In addition, this investigation shows that an updated state parameter definition allows the constitutive model to better model soil response across a range of drainage conditions.

7. Conclusions

Experimental, theoretical and field-case studies have confirmed the occurrence of co-seismic drainage during a liquefaction event in stratified deposits, contradicting the current undrained hypothesis. To understand the importance of drainage across heterogeneous soil layers and accurately model the boundary interactions in numerical analyses, a first step is to assess the capability of advanced constitutive models to replicate element-level behaviour under partial drainage.

The SANISAND family of bounding surface plasticity models are often used to model liquefaction problems. They incorporate the state parameter in the expressions of the bounding and dilatancy surfaces, to make them critical-state compatible. The state parameter (ψ) was defined by Been and Jefferies (1985) as the vertical distance between the current soil state and the critical state line in $e - p'$ space.

In this study, the SANISAND 2008 model performance was evaluated under strain-controlled, coupled strain compression tests, using calibration parameters from undrained and drained monotonic compression tests using the Been and Jefferies (1985) state parameter

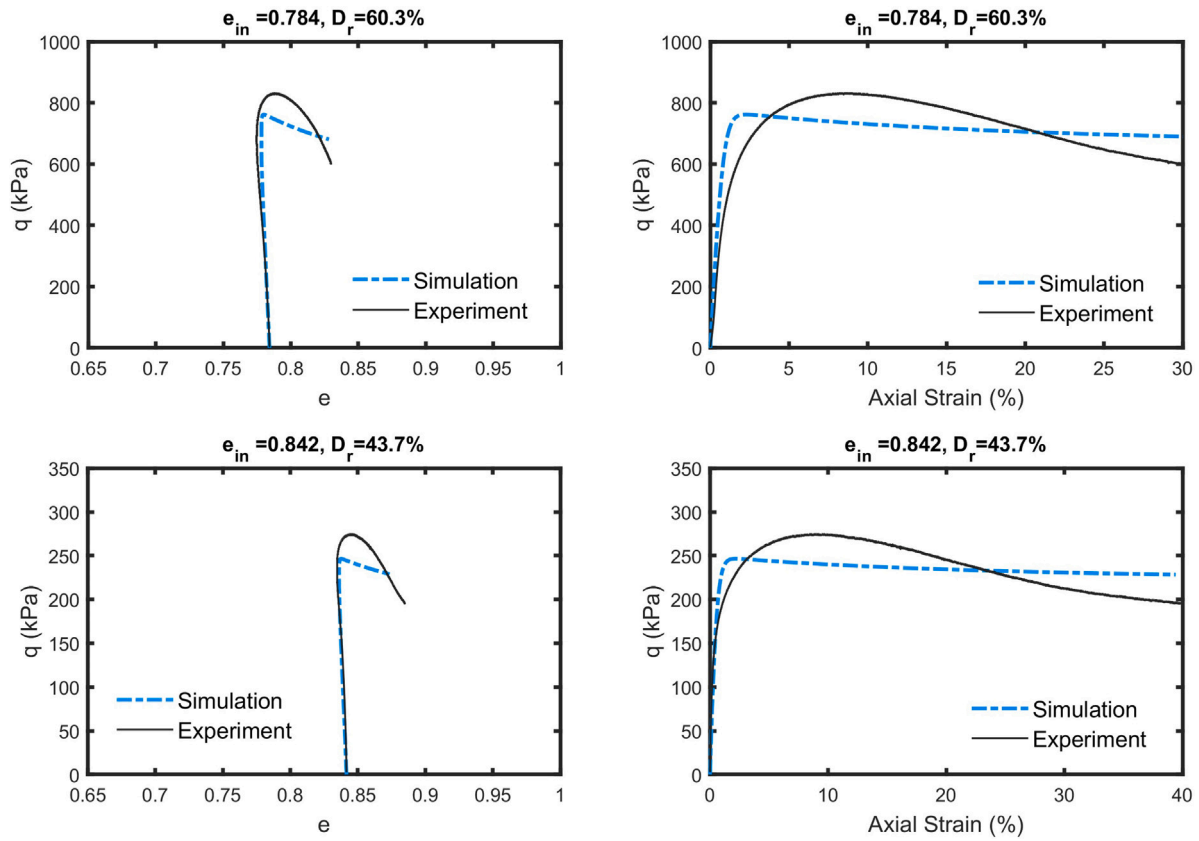


Fig. 28. Simulations of drained monotonic triaxial compression tests on isotropically consolidated samples of Hostun sand using updated ψ_D (Eq. (39)) and comparison with experimental test data (top-bottom: Tests D1 and D4).

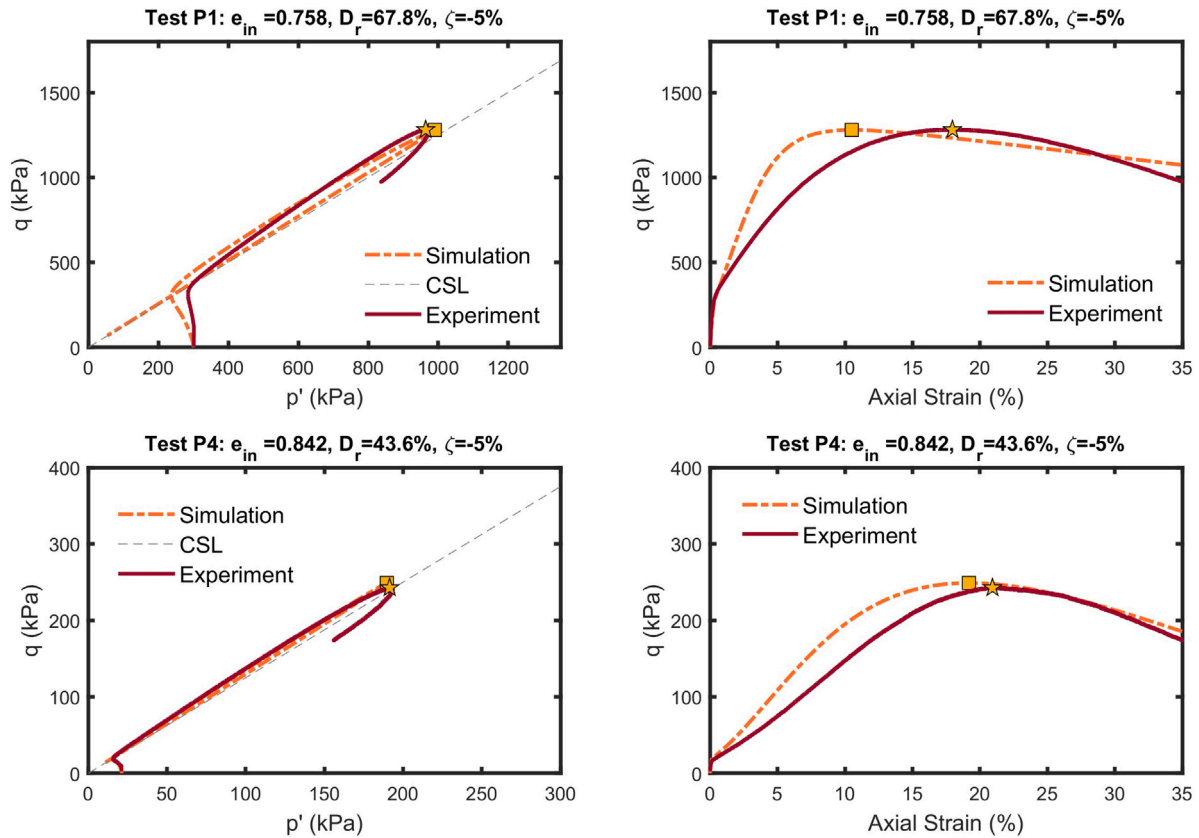


Fig. 29. Simulations of partially drained monotonic triaxial compression tests under $\zeta = -5\%$ on isotropically consolidated samples of Hostun sand using updated ψ_D (Eq. (39)) and comparison with experimental test data.

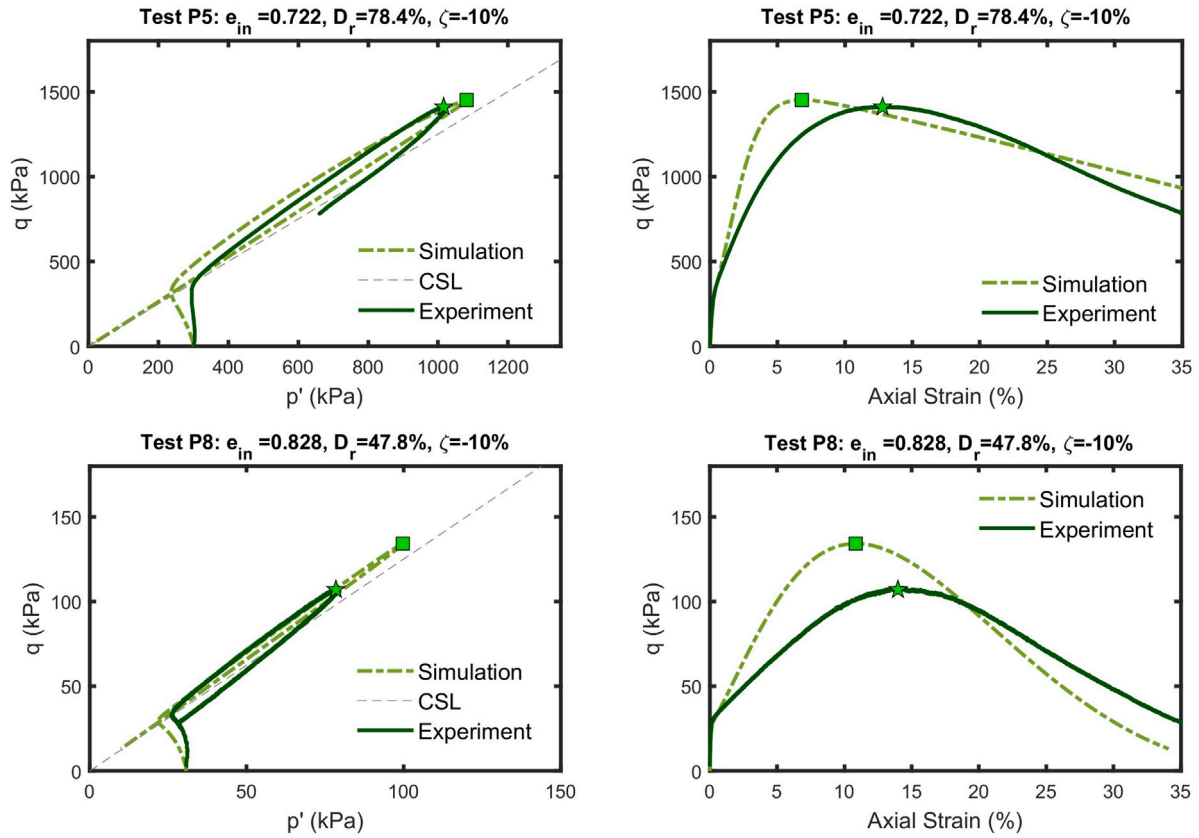


Fig. 30. Simulations of partially drained monotonic triaxial compression tests under $\zeta = -10\%$ on isotropically consolidated samples of Hostun sand using updated ψ_D (Eq. (39)) and comparison with experimental test data.

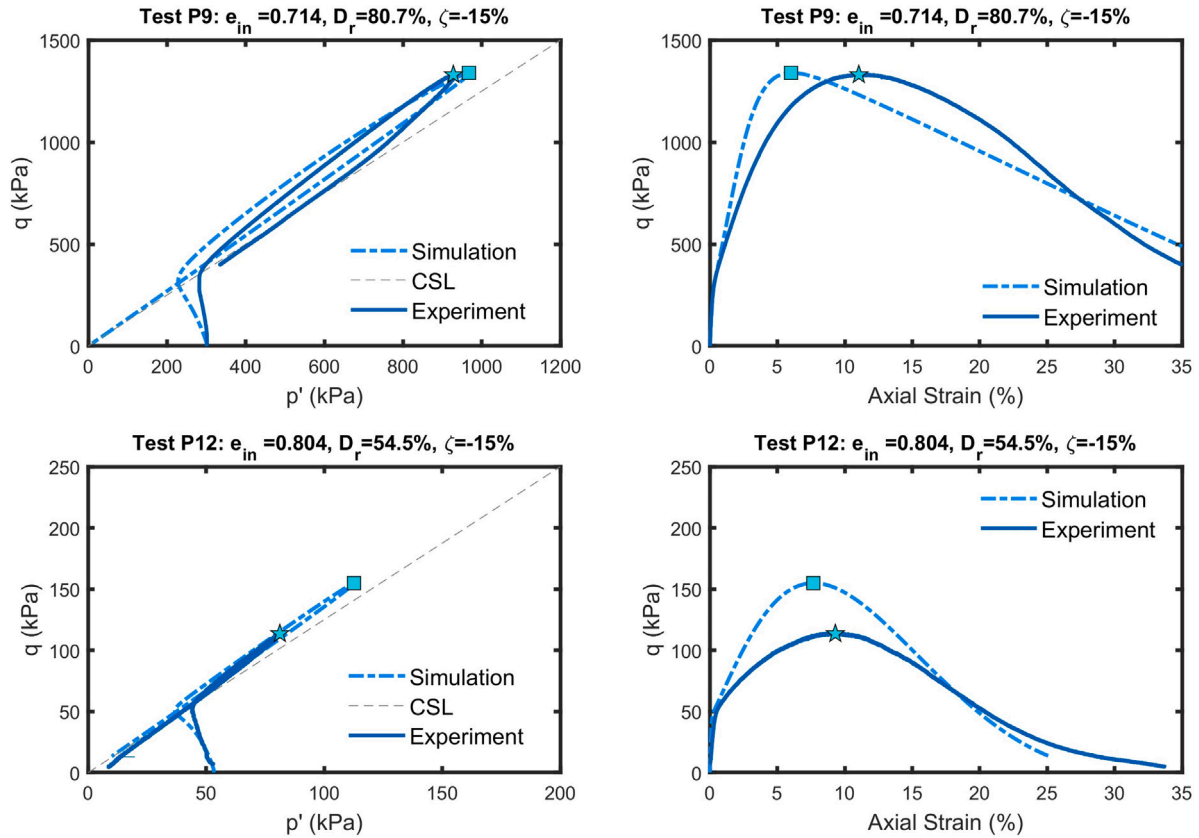


Fig. 31. Simulations of partially drained monotonic triaxial compression tests under $\zeta = -15\%$ on isotropically consolidated samples of Hostun sand using updated ψ_D (Eq. (39)) and comparison with experimental test data.

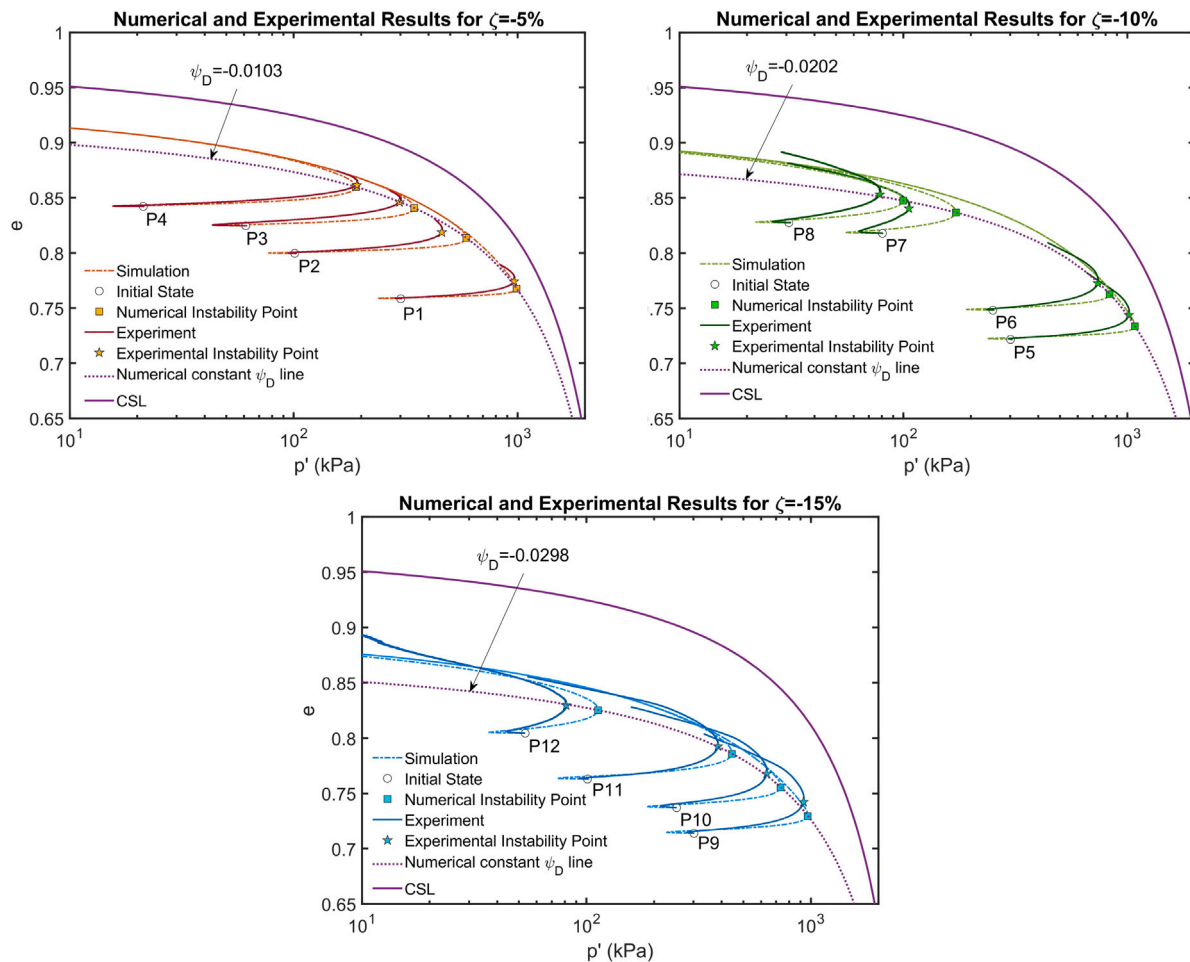


Fig. 32. Simulations of partially drained monotonic triaxial compression tests under $\zeta = -5\%$, -10% and -15% using updated ψ_D (Eq. (39)) in $e - p'$ space and comparison with experimental test data.

definition ψ . Partially drained simulations at element level were conducted by imposing a volumetric strain rate coupled to the axial strain rate. It was analytically demonstrated that for the used constitutive model and a given strain coupling ratio, instability triggering points that violate Hill's stability criterion post phase transformation and post peak stress ratio share the same state parameter ψ . The locus of such instability points (LCSI) was hence shown to fall at a constant value of ψ that depends on the strain coupling ratio.

An experimental campaign was then undertaken to obtain such constant state parameter curves as a way to assess the definition of ψ . Coupled strain monotonic compression tests were conducted for three strain coupling ratios and the post-phase transformation and post-peak instability points were identified. Using the calibrated model parameters, the coupled strain triaxial tests were numerically simulated and it was shown that the locus of numerical instability points in $e - p'$ space, which is at a constant state parameter distance from critical state line, does not coincide with the locus of experimental instability points.

Thus, the performance of the SANISAND 2008 model was found to be deficient in replicating coupled strain paths. An updated state parameter function (ψ_D) was proposed, a constant value of which corresponds to all experimental instability points obtained under the same strain coupling ratio. A re-calibration of the SANISAND 2008 model using ψ_D resulted in a comparably good performance for the drained and undrained test simulations as when using ψ , while a remarkable improvement in performance was observed for the coupled strain paths.

The methodology presented in this study demonstrates how the state parameter definition can be directly assessed using coupled strain

experimental tests. Additionally, this study reveals that an appropriate state parameter is necessary to adequately model partially drained behaviour across a range of initial states.

CRediT authorship contribution statement

Abhinanda Dilip: Conceptualization, Investigation, Methodology, Validation, Writing – original draft. **Orestis Adamidis:** Conceptualization, Supervision, Writing – review & editing.

Declaration of competing interest

The authors declare that they have no known competing financial interests or personal relationships that could have appeared to influence the work reported in this paper.

Data availability

Data will be made available on request.

Acknowledgements

The first author is grateful for the Oxford-Ashton Memorial Graduate scholarship provided by the University of Oxford, that enabled her to pursue this research.

References

- Adamidis, O., Anastasopoulos, I., 2022. Cyclic liquefaction resistance of sand under a constant inflow rate. *Géotechnique* 1–40. <http://dx.doi.org/10.1680/jgeot.21.00082>.
- Adamidis, O., Madabhushi, S., 2018. Experimental investigation of drainage during earthquake-induced liquefaction. *Géotechnique* 68 (8), 655–665. <http://dx.doi.org/10.1680/jgeot.16.P.090>.
- Andrade, J.E., 2009. A predictive framework for liquefaction instability. *Géotechnique* 59 (8), 673–682. <http://dx.doi.org/10.1680/geot.7.00087>.
- Andrade, J.E., Ramos, A.M., Lizcano, A., 2013. Criterion for flow liquefaction instability. *Acta Geotech.* 8 (5), 525–535. <http://dx.doi.org/10.1007/s11440-013-0223-x>.
- Andrianopoulos, K.I., Papadimitriou, A.G., Bouckovalas, G.D., 2010. Bounding surface plasticity model for the seismic liquefaction analysis of geotechnical structures. *Soil Dyn. Earthq. Eng.* 30 (10), 895–911. <http://dx.doi.org/10.1016/j.soildyn.2010.04.001>.
- Azeiteiro, R.J., Coelho, P.A., Tabor, D.M., Grazina, J.C., 2017. Critical State-Based Interpretation of the Monotonic Behaviour of Hostun Sand. American Society of Civil Engineers, [http://dx.doi.org/10.1061/\(ASCE\)GT.1943-5606.0001659](http://dx.doi.org/10.1061/(ASCE)GT.1943-5606.0001659).
- Been, K., Jefferies, M.G., 1985. A state parameter for sands. *Géotechnique* 35 (2), 99–112. <http://dx.doi.org/10.1680/geot.1985.35.2.99>.
- Bolton, M., 1986. The strength and dilatancy of sands. *Geotechnique* 36 (1), 65–78. <http://dx.doi.org/10.1680/geot.1986.36.1.65>.
- Boulanger, R., Ziotopoulou, K., 2015. PM4Sand (Version 3): A Sand Plasticity Model for Earthquake Engineering Applications. Center for Geotechnical Modeling Report No. UCD/CGM-15/01, Department of Civil and Environmental Engineering, University of California, Davis, Calif.
- Bullock, S., Dashti, S., Liel, A., Porter, K., 2022. Physics-informed probabilistic models for peak pore pressure and shear strain in layered, liquefiable deposits. *Géotechnique* 1–14. <http://dx.doi.org/10.1680/jgeot.21.00110>.
- Chu, J., Wanatowski, D., Loke, W., Leong, W., 2015. Pre-failure instability of sand under dilatancy rate controlled conditions. *Soils Found.* 55 (2), 414–424. <http://dx.doi.org/10.1016/j.sandf.2015.02.015>.
- Cubrinovski, M., Ntritos, N., 2023. 8TH Ishihara lecture: Holistic evaluation of liquefaction response. *Soil Dyn. Earthq. Eng.* 168, 107777. <http://dx.doi.org/10.1016/j.soildyn.2023.107777>.
- Cubrinovski, M., Rhodes, A., Ntritos, N., Van Ballegooy, S., 2019. System response of liquefiable deposits. *Soil Dyn. Earthq. Eng.* 124, 212–229. <http://dx.doi.org/10.1016/j.soildyn.2018.05.013>.
- Dafalias, Y.F., Manzari, M.T., 2004. Simple plasticity sand model accounting for fabric change effects. *J. Eng. Mech.* 130 (6), 622–634. [http://dx.doi.org/10.1061/\(ASCE\)0733-9399\(2004\)130:6\(622\)](http://dx.doi.org/10.1061/(ASCE)0733-9399(2004)130:6(622)).
- Grey, L., Adamidis, O., 2024. Liquefaction resistance of medium-dense hostun sand under volumetric contraction. In: 8th International Conference on Earthquake Geotechnical Engineering, Osaka, Japan.
- Hardin, B.O., 1978. The nature of stress-strain behavior for soils. In: From Volume I of Earthquake Engineering and Soil Dynamics—Proceedings of the ASCE Geotechnical Engineering Division Specialty Conference, June 19–21, 1978, Pasadena, California. Sponsored By Geotechnical Engineering Division of ASCE in Cooperation with: (Proceeding).
- Hill, R., 1958. A general theory of uniqueness and stability in elastic-plastic solids. *J. Mech. Phys. Solids* 6 (3), 236–249. [http://dx.doi.org/10.1016/0022-5096\(58\)90029-2](http://dx.doi.org/10.1016/0022-5096(58)90029-2).
- Imposimato, S., Nova, R., 1998. An investigation on the uniqueness of the incremental response of elastoplastic models for virgin sand. *Mech. Cohesive-Frict. Mater.: Int. J. Exp., Model. Comput. Mater. Struct.* 3 (1), 65–87. [http://dx.doi.org/10.1002/\(SICI\)1099-1484\(199801\)3:1%3C65::AID-CFM42%3E3.0.CO;2-9](http://dx.doi.org/10.1002/(SICI)1099-1484(199801)3:1%3C65::AID-CFM42%3E3.0.CO;2-9).
- Ishihara, K., 1993. Liquefaction and flow failure during earthquakes. *Geotechnique* 43 (3), 351–451. <http://dx.doi.org/10.1680/geot.1993.43.3.351>.
- Jefferies, M., 1993. Nor-sand: A simple critical state model for sand. *Géotechnique* 43 (1), 91–103. <http://dx.doi.org/10.1680/geot.1993.43.1.91>.
- Kamai, R., Boulanger, R., 2012. Single-element simulations of partial-drainage effects under monotonic and cyclic loading. *Soil Dyn. Earthq. Eng.* 35, 29–40. <http://dx.doi.org/10.1016/j.soildyn.2011.10.002>.
- Kassas, K., Adamidis, O., Gerolymos, N., Anastasopoulos, I., 2021. Numerical modelling of a structure with shallow strip foundation during earthquake-induced liquefaction. *Géotechnique* 71 (12), 1099–1113. <http://dx.doi.org/10.1680/jgeot.19.P.277>.
- Kikumoto, M., Wood, D.M., Russell, A., 2010. Particle crushing and deformation behaviour. *Soils Found.* 50 (4), 547–563. <http://dx.doi.org/10.3208/sandf.50.547>.
- Kokusho, T., 1999. Water film in liquefied sand and its effect on lateral spread. *J. Geotech. Geoenviron. Eng.* 125 (10), 817–826. [http://dx.doi.org/10.1061/\(ASCE\)1090-0241\(1999\)125:10\(817\)](http://dx.doi.org/10.1061/(ASCE)1090-0241(1999)125:10(817)).
- Konrad, J., 1993. Undrained response of loosely compacted sands during monotonic and cyclic compression tests. *Géotechnique* 43 (1), 69–89. <http://dx.doi.org/10.1680/geot.1993.43.1.69>.
- Lade, P.V., 2016. *Triaxial Testing of Soils*. John Wiley & Sons.
- Lancelot, L., Shahrour, I., Al Mahmoud, M., 2004. Instability and static liquefaction on proportional strain paths for sand at low stresses. *J. Eng. Mech.* 130 (11), 1365–1372. [http://dx.doi.org/10.1061/\(ASCE\)0733-9399\(2004\)130:11\(1365\)](http://dx.doi.org/10.1061/(ASCE)0733-9399(2004)130:11(1365)).
- Lashkari, A., Falsafizadeh, S., Rahman, M.M., 2021. Influence of linear coupling between volumetric and shear strains on instability and post-peak softening of sand in direct simple shear tests. *Acta Geotech.* 16 (11), 3467–3488. <http://dx.doi.org/10.1007/s11440-021-01288-5>.
- Lashkari, A., Yaghtin, M., 2018. Sand flow liquefaction instability under shear-volume coupled strain paths. *Géotechnique* 68 (11), 1002–1024. <http://dx.doi.org/10.1680/jgeot.17.P.164>.
- Li, X.S., Dafalias, Y.F., 2000. Dilatancy for cohesionless soils. *Géotechnique* 50 (4), 449–460. <http://dx.doi.org/10.1680/geot.2000.50.4.449>.
- Malvick, E.J., Kutter, B.L., Boulanger, R.W., 2008. Postshaking shear strain localization in a centrifuge model of a saturated sand slope. *J. Geotech. Geoenviron. Eng.* 134 (2), 164–174. [http://dx.doi.org/10.1061/\(ASCE\)1090-0241\(2008\)134:2\(164\)](http://dx.doi.org/10.1061/(ASCE)1090-0241(2008)134:2(164)).
- Malvick, E.J., Kutter, B.L., Boulanger, R.W., Kulasingam, R., 2006. Shear localization due to liquefaction-induced void redistribution in a layered infinite slope. *J. Geotech. Geoenviron. Eng.* 132 (10), 1293–1303. [http://dx.doi.org/10.1061/\(ASCE\)1090-0241\(2006\)132:10\(1293\)](http://dx.doi.org/10.1061/(ASCE)1090-0241(2006)132:10(1293)).
- Manzari, M.T., Dafalias, Y.F., 1997. A critical state two-surface plasticity model for sands. *Géotechnique* 47 (2), 255–272. <http://dx.doi.org/10.1680/geot.1997.47.2.255>.
- McDowell, G., Bolton, M., 1998. On the micromechanics of crushable aggregates. *Géotechnique* 48 (5), 667–679. <http://dx.doi.org/10.1680/geot.1998.48.5.667>.
- Nicot, F., Daouadji, A., Hadda, N., Jrad, M., Darve, F., 2013. Granular media failure along triaxial proportional strain paths. *Eur. J. Environ. Civ. Eng.* 17 (9), 777–790. <http://dx.doi.org/10.1080/19648189.2013.819301>.
- Papadimitriou, A.G., Bouckovalas, G.D., Dafalias, Y.F., 2001. Plasticity model for sand under small and large cyclic strains. *J. Geotech. Geoenviron. Eng.* 127 (11), 973–983. [http://dx.doi.org/10.1061/\(ASCE\)1090-0241\(2001\)127:11\(973\)](http://dx.doi.org/10.1061/(ASCE)1090-0241(2001)127:11(973)).
- Papadimitriou, A., Limnaiou, T., Chaloulos, Y., 2023. Benefits and pitfalls of advanced numerical modelling in earthquake geotechnical engineering. In: 10th European Conference on Numerical Methods in Geotechnical Engineering, London, UK, Paper, (no. 440), <http://dx.doi.org/10.53243/NUMGE2023-440>.
- Petalas, A.L., Dafalias, Y.F., Papadimitriou, A.G., 2019. SANISAND-FN: An evolving fabric-based sand model accounting for stress principal axes rotation. *Int. J. Numer. Anal. Methods Geomech.* 43 (1), 97–123. <http://dx.doi.org/10.1002/nag.2855>.
- Sivathayalan, S., Logeswaran, P., 2008. Experimental assessment of the response of sands under shear-volume coupled deformation. *Can. Geotech. J.* 45 (9), 1310–1323. <http://dx.doi.org/10.1139/T08-068>.
- Taiebat, M., Dafalias, Y.F., 2008. SANISAND: Simple anisotropic sand plasticity model. *Int. J. Numer. Anal. Methods Geomech.* 32 (8), 915–948. <http://dx.doi.org/10.1002/nag.651>.
- Taiebat, M., Jeremić, B., Dafalias, Y.F., Kaynia, A.M., Cheng, Z., 2010. Propagation of seismic waves through liquefied soils. *Soil Dyn. Earthq. Eng.* 30 (4), 236–257. <http://dx.doi.org/10.1016/j.soildyn.2009.11.003>.
- Vaid, Y.P., Eliadorani, A., 1998. Instability and liquefaction of granular soils under undrained and partially drained states. *Can. Geotech. J.* 35 (6), 1053–1062. <http://dx.doi.org/10.1139/t98-061>.
- Vaid, Y.P., Eliadorani, A., 2000. Undrained and drained (?) stress-strain response. *Can. Geotech. J.* 37 (5), 1126–1130. <http://dx.doi.org/10.1139/t00-036>.
- Verdugo, R., 1992. Characterization of Sandy Soil Behavior Under Large Deformation. (Ph.D. thesis). Department of Civil Engineering, University of Tokyo, Japan.
- Wang, Z.-L., Dafalias, Y.F., Li, X.-S., Makdisi, F.I., 2002. State pressure index for modeling sand behavior. *J. Geotech. Geoenviron. Eng.* 128 (6), 511–519. [http://dx.doi.org/10.1061/\(ASCE\)1090-0241\(2002\)128:6\(511\)](http://dx.doi.org/10.1061/(ASCE)1090-0241(2002)128:6(511)).
- Yang, M., Taiebat, M., Dafalias, Y.F., 2022. SANISAND-MSF: A sand plasticity model with memory surface and semifluidised state. *Géotechnique* 72 (3), 227–246. <http://dx.doi.org/10.1680/jgeot.19.P.363>.
- Yao, Y.-P., Hou, W., Zhou, A.-N., 2009. UH model: Three-dimensional unified hardening model for overconsolidated clays. *Geotechnique* 59 (5), 451–469. <http://dx.doi.org/10.1680/geot.2007.00029>.
- Yao, Y.-P., Liu, L., Luo, T., Tian, Y., Zhang, J.-M., 2019. Unified hardening (UH) model for clays and sands. *Comput. Geotech.* 110, 326–343. <http://dx.doi.org/10.1016/j.compgeo.2019.02.024>.